School of Mechanical, Aerospace and Automotive Engineering

Faculty of Engineering, Environment and Computing

Aerodynamic analysis of the LAN1897 aerofoil

---

by Esther Plaza Rodríguez

under the supervision of Caroline Lambert

A Dissertation submitted for the degree of BEng Aerospace Technology

April 2019

Declaration of originality

This project is all my own work and has not been copied in part or in whole from any other source except where duly acknowledged. As such, all use of previously published work (from books, journals, magazines, internet, etc.) has been acknowledged within the main report to an item in the References or Bibliography lists.

I also agree that an electronic copy of this project may be stored and used for the purposes of plagiarism prevention and detection.

Plaza

Signed: Esther Plaza Rodríguez

Date of submission: 29/04/2019

Acknowledgement

I would like to express my sincerest gratitude to Dr. Caroline Lambert for her involvement and guidance during the development of this project. Without her willingness to supervise me and the offer of this interesting dissertation, none of this would have been possible. It has been a real pleasure working with you.

Also, thank you to my supervisor in the Universitat Politècnica de València, Pedro Manuel Quintero for your willingness to validate my project as well as guiding me through the development of the calculations.

Gracias a mis padres, a mi hermana, a mi familia y a mis amigos, por el apoyo incondicional que me han demostrado en todas las decisiones tomadas, principalmente durante estos últimos cuatro años, así como por la paciencia y el cariño que me han dado siempre. Papá, mamá, todo esto os lo debo a vosotros.

Thank you to all the people I have met during the University stage, it has been a pleasure sharing all these moments with you, both suffering and enjoying the experience that we have gained. Thank you José Miguel, for all the things you do for me.

Finally, a special thank you to the people I have met me during the ERASMUS+ in Coventry.

Abstract

In this project the aerodynamic study of the profile designed by Frederick Lanchester, British engineer, is carried out. The main objective of the analysis is to obtain realistic results through the use of simulations with the StarCCM+ software and measurements taken in the wind tunnel. In this way, it is possible to compare the results obtained, as well as test their reliability.

Since this project is the continuation of a Master’s dissertation (Ugwueze 2017), part of the literature review is omitted, although a part of this information is included in a summarized manner.

Said so, the present dissertation will consist mainly of a theoretical introduction about the historical framework in which the profile was developed, the description of the procedure followed for its elaboration, the detailed analysis of the profile of interest and the presentation and comparison of the results obtained.

Finally, different options will be proposed with which it will be possible to keep developing and complementing the study of the aerofoil, designated as LAN1897 (Ugwueze 2017).

Key Words: CFD, aerofoil, wind tunnel, F. W. Lanchester, StarCCM+, aerodynamics, lift, drag, flow.

Index

Declaration of originality I

Acknowledgement III

Abstract V

Index VII

List of Figures XI

List of Tables XIII

Nomenclature XV

Introduction 1

- 1.1. Motivation and objectives 2
- 1.2. Scope 3
- 1.3. Structure of the dissertation 3

Literature Review 5

- 2.1. F. W. Lanchester’s life 5
- 2.2. Main Contributions 6
- 2.3. Contribution to Aerodynamics 7

Theoretical background 9

- 3.1. Aerodynamic forces and moments 9
  - 3.1.1. Lift 9
  - 3.1.2. Drag 10
- 3.2. Dimensionlessness of the variables 10

3.2.1. Lift coefficient 10
3.2.2. Drag coefficient 10
3.2.3. Pressure coefficient 10
3.3. Boundary Layer 11
3.4. 3-Dimensional Effects 12
3.5. Conservation equations 12
3.5.1. Mass conservation 12
3.5.2. Momentum conservation 13
3.5.3. Energy conservation 13
Aerofoil Analysis 15
4.1. Characteristic curves 16
4.1.1. Lift curve 16
4.1.2. Drag curve 16
Procedure 19
5.1. Manufacturing of the physical model and assembly 19
5.2. CFD Set-up 21
5.2.1. Meshing characteristics 21
Mesh description 21
Boundary conditions 23
Selection of the turbulence model 23
Assumptions 24
Mesh Independence 24
Convergence criteria 25
Validation 27
6.1. CFD results 27
6.1.1. Constant velocity 27
Pressure coefficient distribution 28
Lift curve 30
Drag curve 31
Drag polar curve 31

Angle of attack α = 0° 34
Angle of attack α = 5° 35
Angle of attack α = 10° 36
Angle of attack α = 15° 37
Angle of attack α = 20° 38
6.1.2. Constant angle of attack 39
6.2. Wind tunnel results 40
6.2.1. Constant velocity 41
Lift curve 41
Drag curve 41
Drag polar curve 42
6.2.2. Constant angle of attack 43
Comparison of the results 45
7.1. Lift curve 45
7.2. Drag curve 46
7.3. Drag polar curve 47
7.4. Aerodynamic Efficiency 48
Conclusions 51
Costs 53
Recommendations for further work 55
References and Bibliography 57
Appendices 61
A1. LAN1897 Aerofoil Data 61
A2. Mesh independence 62
A3. Convergence 63
A4. Velocity determination 65
A5. CFD numerical results 66
A6. Wind Tunnel numerical results 67

List of Figures

Figure 1. Examples of aerofoils (The Development of Aerofoils and Aerofoil Technology 2019) 1
Figure 2. F. W. Lanchester with one of his designed gliders, 1894 (Frederick Lanchester Collection 2019). 6
Figure 3. Forces acting on an aerofoil (Anderson 2011). 10
Figure 4. Boundary Layer description (The Science Behind Golf-Ball Dimples 2019). 11
Figure 5. Boundary Layer Detachment (Contel 2016). 11
Figure 6. Generation of wing tip vortices. Three-dimensional effects (Anderson 2011). 12
Figure 7. Plot of LAN1897 aerofoil (Ugwueze 2017) 15
Figure 8. Lift curve for a generic aerofoil (Marco 2017). 16
Figure 9. Drag curve for a generic aerofoil (Marco 2017). 17
Figure 10. Real shape (left) and rectangular approach (right). 20
Figure 11. Wind tunnel experiment. 20
Figure 12. Control volume. 22
Figure 13. Mesh description. 23
Figure 14. Pressure coefficient for different angles of attack. (● - grey) intrados. (● - black) extrados. 29
Figure 15. Evolution of the lift coefficient with respect to the angle of attack (CFD). 30
Figure 16. Evolution of the drag coefficient with respect to the angle of attack (CFD). 31
Figure 17. Evolution of the lift coefficient with respect to the drag coefficient (CFD). 32
Figure 18.Evolution of the aerodynamic efficiency with respect to the angle of attack (CFD). 32
Figure 19. Evolution of the drag coefficient with respect to the aerodynamic efficiency (CFD). 33
Figure 20. Static pressure contour for an angle of attack α = 0°. 34
Figure 21. Velocity contour for an angle of attack α = 0°. 34
Figure 22. Static pressure contour for an angle of attack α = 5°. 35
Figure 23. Velocity contour for an angle of attack α = 5°. 35
Figure 24. Static pressure contour for an angle of attack α = 10°. 36

Figure 25. Velocity contour for an angle of attack α = 10°. 36
Figure 26. Static pressure contour for an angle of attack α = 15°... 37
Figure 27. Velocity contour for an angle of attack α = 15°. 37
Figure 28. Static pressure contour for an angle of attack α = 20°... 38
Figure 29. Velocity contour for an angle of attack α = 20°. 38
Figure 30. Evolution of the drag coefficient with respect to the velocity (CFD). 40
Figure 31. Evolution of the lift coefficient with respect to the angle of attack (Wind Tunnel).... 41
Figure 32. Evolution of the drag coefficient with respect to the angle of attack (Wind Tunnel). 42
Figure 33. Evolution of the lift coefficient with respect to the drag coefficient (Wind Tunnel). . 42
Figure 34. Evolution of the aerodynamic efficiency with respect to the angle of attack (Wind Tunnel)... 43
Figure 35. Evolution of the drag coefficient with respect to the velocity (Wind Tunnel). 44
Figure 36. Lift coefficient curve comparison.. 46
Figure 37. Drag coefficient curve comparison.. 47
Figure 38. Polar drag curve comparison... 47
Figure 39. Aerodynamic efficiency comparison. 48
Figure 40. Aerodynamic efficiency comparison (detail). 49
Figure 41. Residuals at constant velocity and at an angle of attack α = 0°. 63
Figure 42. Lift and Drag monitor plots at constant velocity and at an angle of attack α = 0°...... 63
Figure 43. Residuals at constant velocity and at an angle of attack α = 10°. 63
Figure 44. Lift and Drag monitor plots at constant velocity and at an angle of attack α = 10°.... 64
Figure 45. Residuals at constant velocity and at an angle of attack α = 15°. 64
Figure 46. Lift and Drag monitor plots at constant velocity and at an angle of attack α = 15°.... 64

List of Tables

Table 1. Main characteristics of the aerofoil LAN1897 (Ugwueze 2017). 15
Table 2. Flight conditions. 21
Table 3. Boundary conditions for the initial simulations. 23
Table 4. Lift and drag coefficients from the different meshes.. 24
Table 5. Cost derived from human resources. 53
Table 6. Cost derived from physical resources. 54
Table 7. Parameters for mesh independence. 62
Table 8. Mass Flow conservation. 62
Table 9. CFD parameters at constant velocity. 66
Table 10. CFD parameters at constant angle of attack. 66
Table 11. Wind Tunnel parameters at constant velocity. 67
Table 12.Wind Tunnel parameters at constant angle of attack. 68

Nomenclature

Aerodynamic Efficiency	AE
Angle of Attack	α
Axial Force	A
Chord	c
Density	ρ
Drag Coefficient	C_D
Drag Force	D
Dynamic Viscosity	μ
Freestream Velocity	V_∞
Lift Coefficient	C_L
Lift Force	L
Mach number	Ma
Minimum Drag Coefficient	CD_{min}
Moment	M
Normal Force	N
Pressure	p
Pressure Coefficient	C_P
Resultant Force	R
Reynolds Number	Re
Shear Stress	τ
Span	b
Surface	S
Thickness-to-chord ratio	t/c
Zero angle lift Coefficient	CL_0
Zero lift drag Coefficient	CD_0

Introduction

Aerofoil is the name received by the cross-sectional shape of the objects which create an aerodynamic force when moved through the air (*Aerofoil – Aviationknowledge* 2019). Aerofoils are one of the most important elements to consider in aerodynamics, offering the best ratios for the efficiency. To know the origin of aerofoils, it is necessary to go back several centuries ago.

The first antecedent for aerofoil were flat plates. They could create a sideways force, nowadays known to be the lift force. Even if the concept of aerodynamic forces did not exist as it does nowadays, there were those interested in flying and developing flying machines, such as Leonardo Da Vinci, George Cayley, Otto Lilienthal or Frederick Lanchester, amongst others.

For researchers up to the 19th century, the source of ideas was the wildlife. Experiments and models were based on animals' physiognomy such as bats, albatrosses or birds. However, it was during this century that more complex aerofoils were designed, thanks to the advance in engineering (Hortsmann and Boermans 2003).

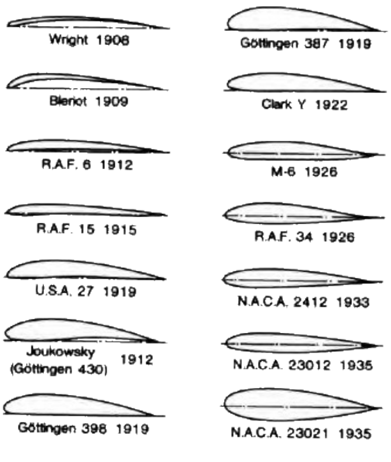

Figure 1. Examples of aerofoils (*The Development of Aerofoils and Aerofoil Technology* 2019)

During the second decade of the 20th century, the need for designing more efficient aerofoils arose, mainly due to the increase of popularity of the aircrafts. In this way, the National Committee on Aeronautics (NACA) appeared. From that moment, the development of aerofoils has not stopped, with the appearance of several criteria to define their shape and the way they make the flow to behave (*The Development of Aerofoils and Aerofoil Technology* 2019).

1.1. Motivation and objectives

The interest shown towards aerofoil design emerged after studying subjects such as Advanced Fluid Dynamics, Aerodynamics and Aerospace Technology, included within the degree course and at which the basic concepts and tools were introduced to the students.

Furthermore, the present project was an opportunity to develop a deep study using both experimental and numerical methods, so that the results obtained could be contrasted.

Finally, knowing the influence that F. W. Lanchester had on various fields of the engineering and his repercussion in the industry developed in the United Kingdom during the 19th and 20th centuries highlighted the interest on this project.

The case study that is going to be faced in this project, as stated in the *Abstract*, will be the comparison between the Computational Fluid Dynamics (CFD) and experimental procedures in the wind tunnel of Lanchester's LAN1897 aerofoil, considering different flight conditions.

Thus, this report shall analyse two main different cases. The first one will be contemplating a change in the angle of attack seen by the aerofoil, from a null angle until the calculated stall angle of attack and a higher value to check which the effects of stall are. The second one will be considering a change in the velocities, from the stall velocity to the flight velocity used in the simulations (Ugwueze 2017).

Therefore, the main objectives that this project aims to fulfil are:

- Complementation of the previous study performed (Ugwueze 2017).
- Analysis of the behaviour of the flow in the different configurations by means of two approaches.
- Validation and comparison of the results obtained by means of both the numerical and the experimental method.
- Evaluation of the limitations and strengths of the aerofoil designed by F. W. Lanchester.

1.2. Scope

The most remarkable tasks that have been carried out in this project are:

- 3D Computer Aided Design (CAD) of the LAN1897 aerofoil using Autodesk Fusion 360.
- Construction of the physical model for the aerofoil with a 3D printer.
- CFD analysis of the aerofoil.

1.3. Structure of the dissertation

The process defined will be detailed in the chapters to come as follows:

- Chapter 1, Introduction, performs a general description of the project.
- Chapter 2, Literature Review, introduces the historical context at which Lanchester developed his theory.
- Chapter 3, Theoretical background, describes the basic concepts used along the dissertation.
- Chapter 4, Aerofoil analysis, offers a complete description of the aerofoil that Lanchester designed, both aerodynamically and structurally.
- Chapter 5, Procedure, provides the steps followed to build the prototype and the performance of the simulations.
- Chapter 6, Validation, presents and discusses the results obtained from the CFD simulation and the wind tunnel's measurements.
- Chapter 7, Comparison of the results, provides a deep analysis and correlation between the results obtained by means of both methods.
- Chapter 8, Conclusions, provides the technical conclusions of the extracted results and a general assessments of the project in general.
- Chapter 9, Costs, offers and approach of the total costs arisen from the development of the project.
- Chapter 10, Recommendations for further work, is summary of the proposed tasks to be performed for a further analysis of the LAN1897 aerofoil.

Literature Review

Nowadays, Frederick William Lanchester is considered to be one of the most respected aerodynamicists of his time. His contributions led to the development of the theoretical aerodynamics. Nevertheless, despite the analysis that he performed and the advances that he achieved, his merits were never recognised when published due to his poor writing style and the lack of mathematical background provided in his publications (Jarrett 2014).

This chapter provides a brief overview of F. W. Lanchester's life and his contributions to aerodynamics.

2.1. F. W. Lanchester's life

Lanchester was born in London in 1868, son of an architect (Henry Jones Lanchester) and a tutor of Latin and Mathematics (Octavia Ward). When he was a child, his family decided to move to Brighton for labour reasons, where he attended a school in the East part of the city without showing any special interest or brilliance (Lanchester 1955).

At the age of 14, Lanchester was sent to Hartley Institute, where he studied engineering. After this period, he won a scholarship to the Normal School of Science and School of Mines, where his outstanding brilliance arose. At the same moment, he started combining his formal studies with evening lectures to gain practical knowledge (Jarret 2014). In his third, and therefore final, year in the School of Science, he built a telescope. Nevertheless, due to the dissatisfaction with the result obtained, he decided not to attend the end-of-year exam in order to have another year to perform improvements. He finally left the School without any official qualification (*Frederick Lanchester Collection* 2019).

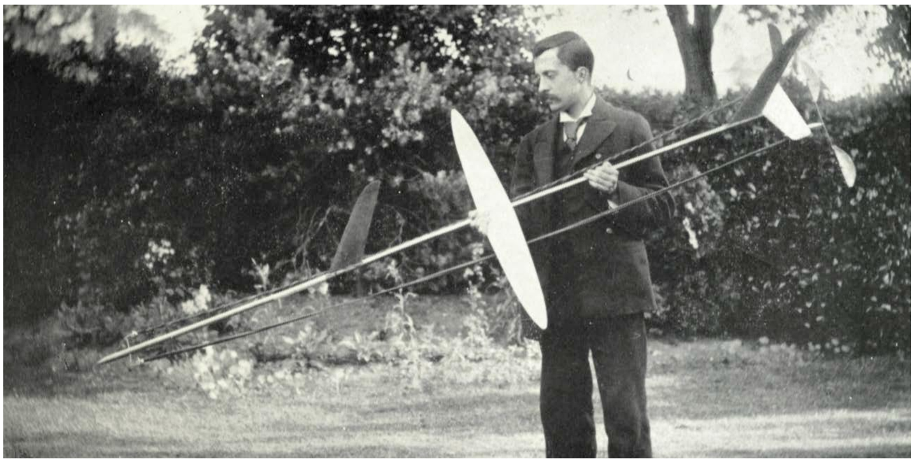

Figure 2. F. W. Lanchester with one of his designed gliders, 1894 (*Frederick Lanchester Collection* 2019).

In 1888 he accepted a job in a Patent Office. It is during this period when he obtained his first patent, the isometrograph. By the end of 1888, he started working in Forward Gas Engine Company, re-designing and updating a whole range of the engines that were being produced. After two years, Frederick became Works Manager and began researching and developing new ideas for motor vehicles. One of these engines was used to create the first British motorboat, piloted on the River Thames at Oxford (Lanchester 1955).

During these years, road restrictions had been implemented in United Kingdom. It is between 1894 and 1895 when Lanchester decides to quit his job and designs his first motor car, taking as a reference the models built in France and Germany, where no road restrictions existed. In 1899 he founded the Lanchester Engine Company with the assistance of his brothers, George and Frank, with the factory located in a suburb of Birmingham. In 1904, due to financial issues, the company was reconstructed as Lanchester Motor Company and it is from this moment that Frederick is able to combine his interests in both cars and flight (*Frederick Lanchester Collection* 2019).

In his later life, Frederick studied anatomy – mainly related to eyesight experiments – due to the vision loss that he was experiencing.

2.2. Main Contributions

From the moment he patented his first invention until his death in 1946, F. W. Lanchester applied for a total of 440 patents, being successful with 230 of them (*Frederick Lanchester Collection* 2019). Some of his most remarkable patents were:

- Patent for an improved apparatus for ruling parallel equidistant lines and for like purposes, 13 November 1888.
- Patent for improvements in and relating to aerial machines, 10 February 1897.
- Patent for improvements in the steering and controlling mechanism of power propelled vehicles, 02 February 1903.
- Patent for improvements in power propelled road vehicles, 02 August 1904.
- Patent for improvements relating to the propulsion of vehicles by combustion of prime mover and electrical storage, 08 August 1910.

2.3. Contribution to Aerodynamics

In 1892, F. W. Lanchester formulated the vortex theory of sustentation, building several models in order to prove it. This represented the basis of aerodynamics, as well as the starting point for modern aerofoil theory. Between 1907 and 1908 he published his two most famous works Aerodynamics and Aerodonetics (Lanchester 1955), at which he developed the full description of lift and drag and the study of oscillations and stall, respectively. His findings were not well received in United Kingdom, whereas it was a German scientist, Ludwig Prandtl, who mathematically proved how correct he was with his theories.

Theoretical background

Attending to the definition of aerodynamics as the science that studies the movement of gases and the way solid bodies move through them (Glauert 1930), it is clear that forces will play an important role in the study of this branch of the engineering.

It is necessary to define various concepts in order to acquire a complete understanding about the parameters that are analysed in the report. In this chapter, these concepts will be described.

3.1. Aerodynamic forces and moments

The aerodynamic forces and moments that arise on a body are due to two main reasons: the pressure and the shear stress distribution over its surface. Thus, pressure (p) acts normal to the surface whereas the shear stress (τ) acts perpendicularly (Anderson 2011). Furthermore, if the net effect of their distribution is calculated, a resultant force (R) and a moment (M) appear. This force can be further divided in two different components: axial (A) and normal (N) forces, which are defined by their relative position to the freestream velocity. Also, given an existing angle between the velocity vector and the chord of the aerofoil, two more components of the force appear: lift and drag.

3.1.1. Lift

It is the component of R perpendicular to the freestream velocity (Anderson, 2011). Taking into account the geometrical relation between the components, it can be expressed as:

$$\mathrm{L} = \mathrm{N}\cos\alpha - \mathrm{A}\sin\alpha \tag{3.1}$$

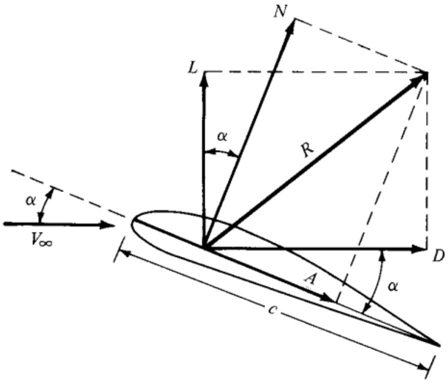

Figure 3. Forces acting on an aerofoil (Anderson 2011).

3.1.2. Drag

It is the component of R parallel to the freestream velocity (Anderson 2011). It can be expressed as:

$$D = N\sin\alpha + A\cos\alpha \tag{3.2}$$

3.2. Dimensionlessness of the variables

Once the results of the behaviour of the flow around the aerofoil are obtained, it is always interesting being able to compare such values with others found when changing boundary conditions or geometries. In order to do so, it is necessary to work with dimensionless coefficients (Marco 2017).

3.2.1. Lift coefficient

$$C_L = \frac{2\,L}{\rho\,V^2\,S} \tag{3.3}$$

3.2.2. Drag coefficient

$$C_D = \frac{2\,D}{\rho\,V^2\,S} \tag{3.4}$$

3.2.3. Pressure coefficient

It allows obtaining the pressure distribution on the aerofoil surface, considering the value of the local pressure in each point and the static pressure in the freestream.

$$C_P = \frac{p - p_\infty}{\frac{1}{2}\rho V^2} \tag{3.5}$$

3.3. Boundary Layer

When the undisturbed flow intersects an obstacle, in its vicinity the thermodynamic and velocity fields are affected. The area where the properties of the fluid are altered by the close presence of the solid body is known as boundary layer (Puttkammer 2013).

The behaviour of the flow in the boundary layer is very important because it has a great influence in different phenomena such as stall. Close enough to the body (considered to be a wall), it is generally assumed that the no-slip condition applies, since no velocity will be found at this point. Nevertheless, the velocity gradient will be increasing as the distance to the body increases, too.

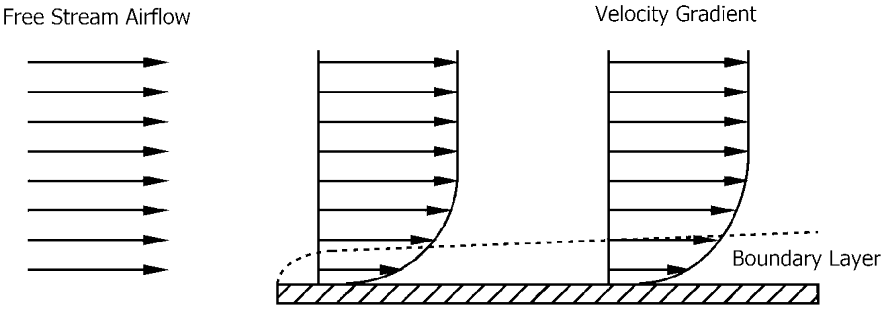

Figure 4. Boundary Layer description (*The Science Behind Golf-Ball Dimples* 2019).

In this region, there can be produced the boundary layer detachment. It is produced when the area which is located closest to the body is immersed in a reversed flow. When the boundary layer detaches, the pressure on rear part of the body is essentially constant. This fact will be analysed in sections to come.

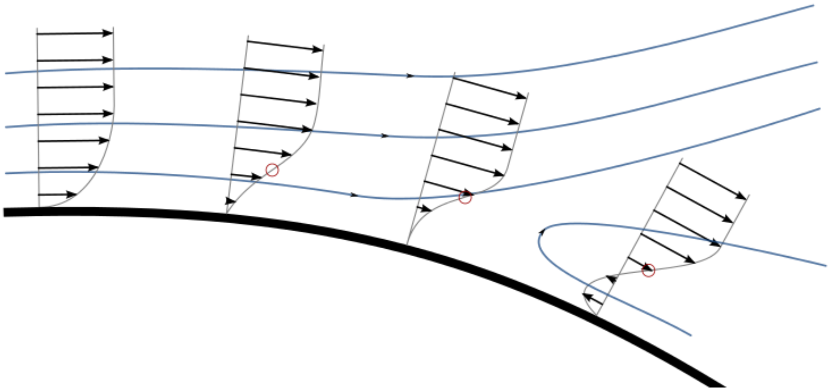

Figure 5. Boundary Layer Detachment (Contel 2016).

3.4. 3-Dimensional Effects

When talking about wings, finite dimensions are being used. Its implications are that a spanwise component of the flow appears, provoking a different behaviour with respect to the 2D homologue aerofoil. This behaviour change is mainly due to the tendency that the flow adapts to curl around the tips of the aerofoil, as seen in Figure 6 (Anderson 2011).

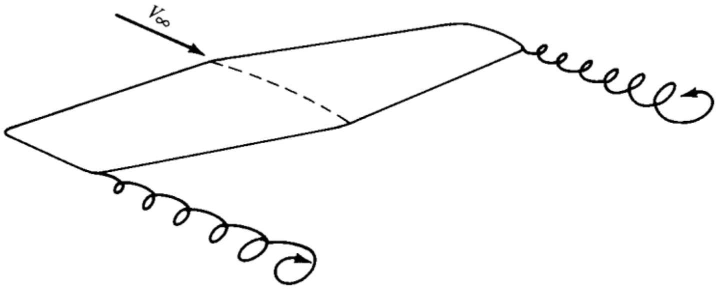

Figure 6. Generation of wing tip vortices. Three-dimensional effects (Anderson 2011).

As for the parameters that will be affected by this consideration, pressure is the one whose implications will have the highest repercussion in the results obtained. One of the conditions that must be accomplished is that no pressure difference will be found in the wing tip, since it is the point at which both extrados and intrados coincide. This produces the displacement of particles from the extrados to the intrados, producing the wing tip vortices just mentioned.

Since the lift is a direct consequence of pressure difference and distribution, its values will differ numerously depending on the approach that is being made, as it will be seen in the following sections.

3.5. Conservation equations

In order to deal with the problems by means of numerical methods, it is necessary to define the set of equations that will be solved in each of the cells of the mesh. These will be the equations that StarCCM+ will be solving in each of the iterations undertaken.

3.5.1. Mass conservation

Once the control volume is defined, mass conservation must be accomplished. It is also known as continuity equation. In an integral form, this statement is defined as follows (Marco 2016):

$$\frac{\mathrm{d}}{\mathrm{dt}}\int_{V_f}\rho(\vec{x},t)\,\mathrm{dV} = \frac{\mathrm{d}}{\mathrm{dt}}\int_{V_c}\rho(\vec{x},t)\,\mathrm{dV} + \int_{S_c}\rho(\vec{x},t)\,(\vec{u}-\vec{u}_c)\,\vec{n}\,\mathrm{d}S \tag{3.6}$$

From left to right, each of the terms represent:

1) Variation with time of the mass linked to a fluid volume.
2) Variation with time of the mass in a control volume.
3) Net mass flow through the surface of such control volume.

The expression provided can be simplified assuming that the flow is not going to be deformed with time. Next, by applying Gauss' theorem, the following equation is found:

$$\frac{\partial \rho}{\partial t} + \nabla \cdot (\rho\, U) = 0 \tag{3.7}$$

3.5.2. Momentum conservation

The equation that defines this requirement is expressed in a differential form and it is obtained by combining the Navier-Poisson Law about viscous stresses in a Newtonian flow and Stokes Law (Marco 2016). This is the reason why it is also known as Navier-Stokes equations:

$$\rho \frac{D\bar{u}_i}{Dt} = -\frac{\partial p}{\partial x_i} + \frac{\partial}{\partial x_j}\left[\mu\left(\frac{\partial u_i}{\partial x_j} + \frac{\partial u_j}{\partial x_i}\right)\right] - \frac{2}{3}\mu\frac{\partial}{\partial x_i}\left(\frac{\partial u_k}{\partial x_k}\right) + \rho\vec{f}_{mi} \tag{3.8}$$

They cannot be solved analytically.

3.5.3. Energy conservation

Energy equations are out of the scope of this project, because the models used and the assumptions made will not be requiring such equations to be solved. In that way, calculations will be easier to be solved. The reason not to set these equations is that, in subsonic regime, the variables are decoupled from the previous equations (Marco 2016).

Aerofoil Analysis

The objective of this chapter is to analyse the aerofoil that was designed by F. W. Lanchester. From the Patent issued in February 1897, *Patent for improvements in and relating to aerial machines* (*Frederick Lanchester Collection* 2019), it is possible to see how the original aerofoil was designed. Its most important characteristics were already analysed and are summarised in Table 1 (Ugwueze 2017).

Table 1. Main characteristics of the aerofoil LAN1897 (Ugwueze 2017).

Characteristic	**Description**
Type	Un-symmetric
Camber	6.9%
Position of camber from the leading edge	27.27%
Maximum Thickness	8.64%

The aerofoil is considered to be an unsymmetrical model with a positive camber. It is important to outline the fact that it is a double cambered aerofoil, meaning that the mean camber line falls both above and below its chord. It was described by Lanchester himself to be 'a convex upper [surface] and a concave under surface', which is the description of a cambered aerofoil (Ugwueze 2017). Also, if the thickness is considered, it can be classified as a medium aerofoil (García-Cuevas and Quintero 2018), so that it will be half way between a thick aerofoil – offering higher lift – and a thin one – having a higher critical Mach number.

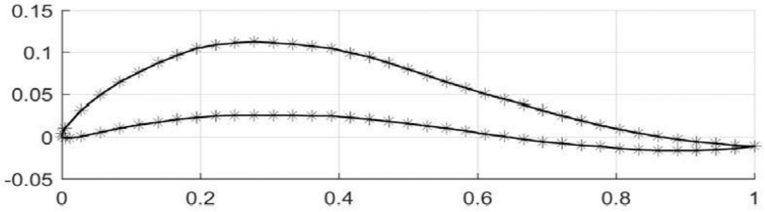

Figure 7. Plot of LAN1897 aerofoil (Ugwueze 2017).

Although the main coefficients of the aerofoil were already calculated using X-Plane's Airfoil Maker, these values are compared with the ones found using Star CCM+ and the wind tunnel measurements, as seen in Chapters 7 and 8. By doing so, more accuracy is reached, since the values obtained by the 2D approach with a flight simulator may entail certain error.

4.1. Characteristic curves

The characteristic curves of an aerofoil do not only depend on the angle of attack at which it is being analysed, but they also depend on parameters such as its shape, the reference area, the speed of the flow and the density of the air.

4.1.1. Lift curve

This characteristic curve provides the variation of the lift coefficient with respect to the angle of attack. Its theoretical slope is 2π, although real aerofoils suffer changes with respect to this ideal value. The lift curve undergoes a linear increase up to a certain value for the angle of attack, at which it suffers a sudden decrease due to the separation of the airflow from the upper surface of the aerofoil. The point at which this decrease occurs is the stall and represents a loss of lift.

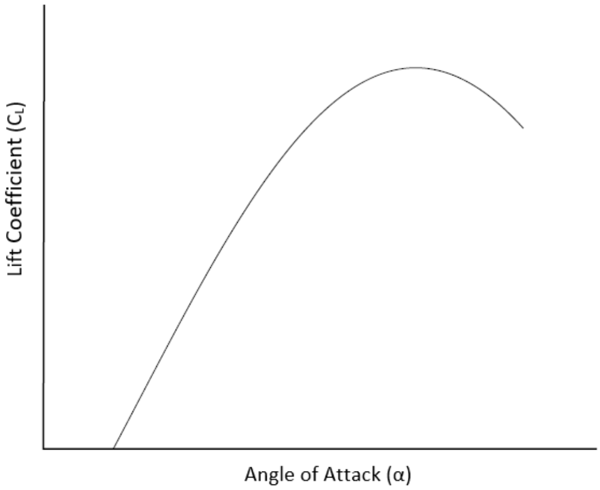

Figure 8. Lift curve for a generic aerofoil (Marco 2017).

4.1.2. Drag curve

As with the lift curve, it also represents the variation of the drag coefficient with respect to the angle of attack. According to the equation for the drag coefficient, it is the result of the combination of the parasitic, wave, pressure and the lift-induced drag. In the most general case, the wave does not play an important role. Thus, the final form of the drag coefficient is ruled by a quadratic equation.

It is also possible to represent the drag curve using as a reference the variation of the velocity instead of the angle of attack. Said so, the graphic is regulated by a quadratic equation as well, resulting of the sum of the two types of drag remaining. It can be seen that the descending branch is governed by the lift-induced drag, whereas the ascending one is ruled by the parasitic drag. An interesting point to outline is that the minimum value for the drag will be reached when both the lift-induced and the parasitic drag have the same value.

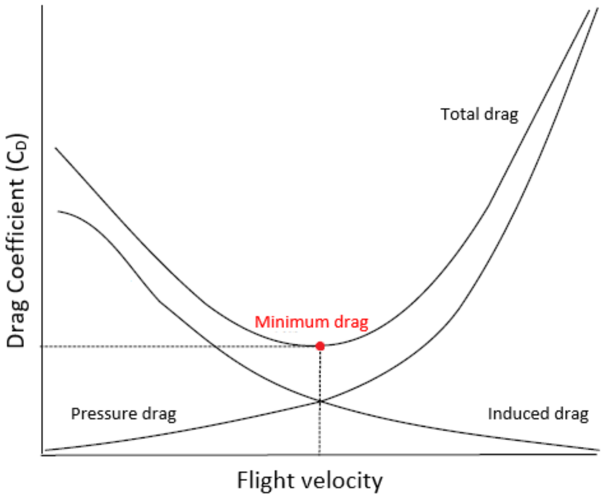

Figure 9. Drag curve for a generic aerofoil (Marco 2017).

Procedure

This project required the design of the aerofoil using a 3D model, for both the experimental and the numerical method. To do so, using the Appendix A1 (Ugwueze 2017), it was possible to locate the points that conformed the aerofoil.

One of the advantages that Autodesk Fusion offers is the possibility to install certain codes already programmed to implement new functionalities. One of such codes is *Airfoil DAT to Spline*, which is able to transform a series of points into a set of splines, creating the shape of the aerofoil.

5.1. Manufacturing of the physical model and assembly

Once the aerofoil is defined, the next step is to extrude it to create the 3D model. Although it was possible to extrude it according to the original shape of the aerial machine (Ugwueze 2017), this would only lead to error while comparing the results from CFD and wind tunnel. Thus, since the most important point of this project is analysing the aerofoil, it is simpler to consider the wing to be rectangular.

In terms of the length extruded, the value used corresponds to the semi span calculated for the aerial machine (Ugwueze 2017).

Due to the size of the 3D printers in the University, it has been necessary to split the wing in two smaller parts and then stick them together by means of a high strength glue: *Gorilla Glue*. This, together with the control volume available in the wind tunnel, has led to a final scaling factor of 1:10.

Figure 10. Real shape (left) and rectangular approach (right).

While undertaking the wind tunnel measurement, it is necessary to add the attachments to fix it and the rod to enable the pitching moment. Once these steps are accomplished, the next step is finding the velocity at which the experiment will be held. The calculation for the velocity can be found in Appendix A4.

According to the theory (Patel et al. 2014; Sendar et al. 2012), the most important point so that the results are representative and comparable is that the Reynolds number is kept constant, or at least the flow regime (laminar or turbulent). Thus, attending to the scaling factor and assuming that dynamic viscosity and air density are the same in both the experiment and the simulations, the velocity in the wind tunnel shall be 10 times higher the one in the simulations. Such value is unconceivable in wind tunnels with the characteristics provided by the available one. Therefore, even when the experiment is performed, this is a factor to be taking into account while discussing and comparing the results.

Figure 11. Wind tunnel experiment.

As it can be seen in Figure 11, the wing is placed in the wind tunnel in the same position as a Formula 1 aileron, downwards. The reason for doing so is having the flow in the extrados the least disturbed as possible, as it is the most important part of the wing and the attachments had to be in the upper part of the structure. Since the wing is placed downwards, the results will be displaying that it generates a downforce instead of positive lift. Consequently, it will be necessary to manipulate the results acquired and represent them as if the wing was placed upwards.

5.2. CFD Set-up

In this section, the flight conditions for the simulations will be presented. According to the data used in previous works, a turbulent Reynolds number shall be used. Also, it is assumed that the atmospheric conditions affecting the results are being considered at sea level.

Flying conditions are summarised in Table 2. The flow is laid out to be incompressible, as velocities are far from the Mach number 0.3, used as a threshold to define compressible flow. Reference values for the pressure are not important in the cases to be studied.

Table 2. Flight conditions.

Parameter	**Value**	**Units**
Altitude	0 (Sea Level)	m
Density	1.225	kg/m^3
Pressure	101325	Pa
Dynamic Viscosity	$1.855 \cdot 10^{-5}$	Pa·s

In the first set of simulations, a velocity of 22.16 m/s is applied, obtained from the condition that the value of for the Reynolds number shall be $1.5 \cdot 10^6$ (Ugwueze 2017).

In the second set of simulations, the velocity is changed between a range from 5 m/s up to 35 m/s. It must be kept in mind that the values reached for the second part of the analysis are just a part of the broadening of the study. It is incorrect to use the assumption of incompressible flow for velocities at which the Mach number is above 0.3. Therefore, in order to avoid errors and data mixing – different models and set up should be used – only the tendency governed by the parasitic drag (low speeds) will be analysed.

5.2.1. Meshing characteristics

Meshing is the basis for CFD simulations. In this section, the main parameters that have been used and the criteria followed to use them will be described.

Mesh description

Defining the meshing area needs to consider to different parameters: the shape of the control volume and the dimensions. In terms of the shape, to save as much computational cost as possible, the control volume is defined combining a semi-circumference in the inlet with a rectangle in the test area. Figure 12 offers the general layout that the control volume will present.

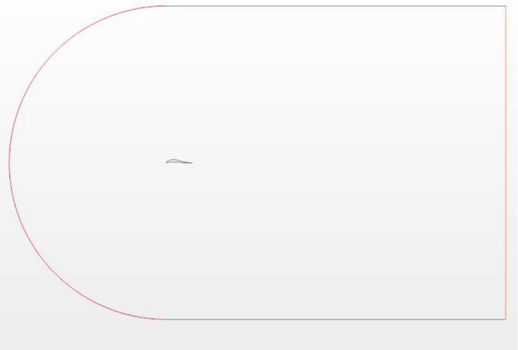

Figure 12. Control volume.

As for the dimensions, the following criteria is used in order to avoid the boundary conditions affecting the results obtained:

- Distance from the inlet to the leading edge: 6 chords.
- Distance from the trailing edge to the outlet: 12 chords.
- Distance from the extrados to the upper wall: 6 chords.
- Distance from the intrados to the lower wall: 6 chords.

Three different types of meshing are used in the control volume: around the aerofoil, in the far field and in the wake. Since it is in the area closer to the aerofoil where the most important data must be calculated, it is decided that prism layers are used around it, due to the accuracy of the results that are obtained using them. Also, the cells suffer a stretching as they become closer to it. Finally, the mesh in the wake has been refined, since flow detachment may occur in this part of the control volume. All these considerations can be observed in Figure 13. It is decided the unstructured mesh type due to the freedom while choosing the geometry of the cells, even if it may require larger storing memory for the simulations (Ferrero 2017).

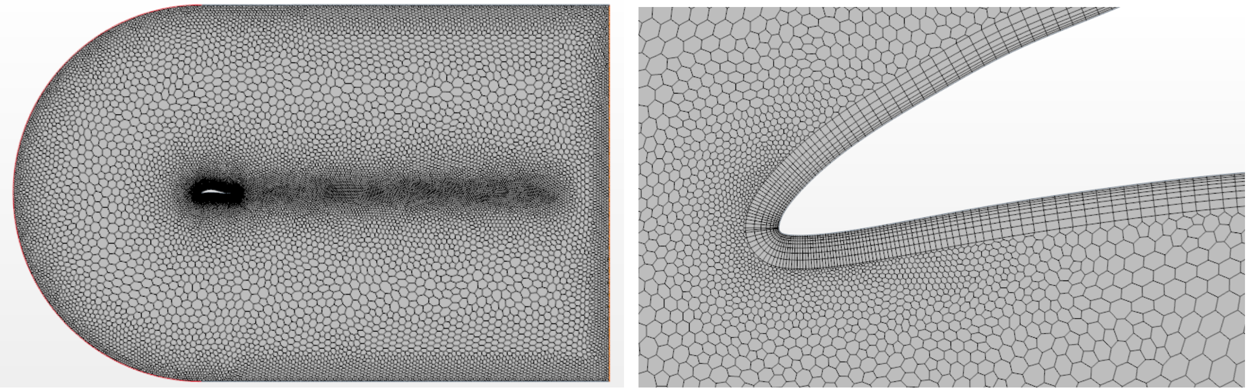

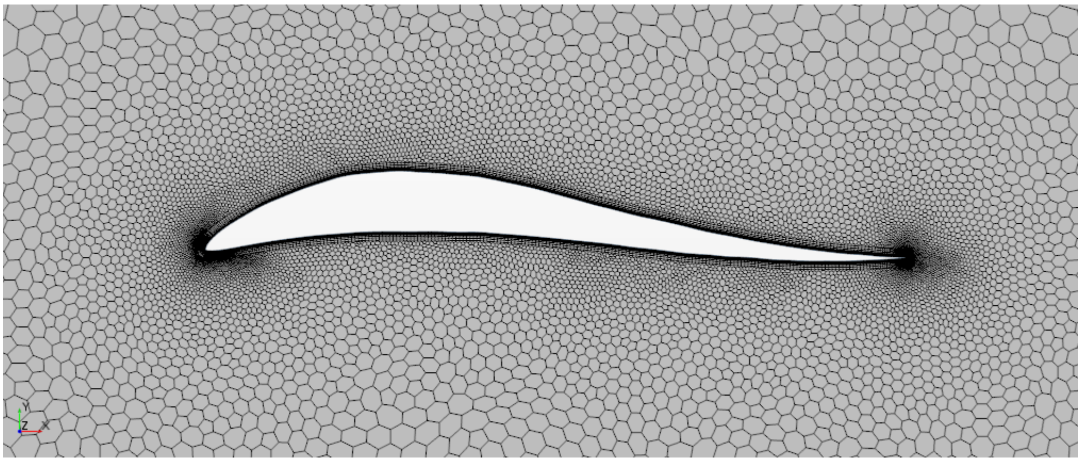

Figure 13. Mesh description.

Boundary conditions

After the creation of the mesh has been finished and prior to solve the transport equations that govern the problem, it is necessary to define the boundary conditions so that a single solution is obtained. It is necessary that the problem is properly defined by means of such boundary conditions, since they will be defining the fluid field that will be analysed. By default, all the surfaces are considered to be walls: stationary wall, no slip condition, standard roughness and no heat flux through it. Nevertheless, it is necessary to change the conditions in both the inlet and the outlet of the control volume, using velocity inlet and pressure outlet, respectively.

Table 3 summarises the parameters for the boundary conditions selected.

Table 3. Boundary conditions for the initial simulations.

Type of boundary condition	Characteristic Parameter	Value	Units
Velocity inlet	Velocity	20	m/s
Pressure outlet	Pressure	101325	Pa

Selection of the turbulence model

The Spalart Allmaras turbulence model is designed specifically for aerospace applications, mainly when the flow is turbulent where vorticity is present (Spalart and Allmaras 1992). It formulates a single partial differential equation which applies both the incompressible and compressible flows. At the same time, the variable that is transported in this model is ν, which can be assimilated to the turbulent kinematic viscosity in the regions that are not affected by strong viscous effects.

Assumptions

Several simplifications are assumed in the CFD analysis. First of all, it is considered to be steady state, which implies that the properties (intensive or extensive) within the control volume do not have variation along time. Furthermore, the flow has been considered to be 2D to obtain a general view of the phenomena occurring in the aerofoil, although the results may be extrapolated to the 3D case.

Also, it is assumed that the gas is ideal and coupled. Based on bibliographical references (Thévenin and Janiga 2008; Wendt 2009; Shaari and Awang 2015) and taking into account the speeds that will be used, the flow is considered to be turbulent, too. Moreover, no compressibility effects will be expected, what allows removing the energy equation from the calculations.

Mesh Independence (Team 2018; *Meshing – CFD wiki* 2019)

The mesh independence is one of the fundamental steps in CFD analysis, since it ensures that the accuracy of the solutions is the highest possible and keeps the computational costs low. The procedure followed in order to perform the study is developing different meshes at which the quality and the number of the cells has been increased according to the refinement needed around the aerofoil and the wake.

The number of cells and the values obtained for the lift and drag coefficients are presented in Table 4. The eight meshes generated have been considered to give satisfactory results in terms of the standard wall function approach when using the Spalart Allmaras model (Patel et al. 2014).

Table 4. Lift and drag coefficients from the different meshes.

Number of cells	C_D (-)	C_L (-)
2 573	0.2605	1.3161
6 862	0.2379	1.2845
10 044	0.2367	1.2882
16 353	0.2008	1.3182
17 448	0.1997	1.3007
20 372	0.1989	1.3216
27 094	0.2078	1.3007
28 740	0.2015	1.2837

Taking into account the results that obtained and the time invested in each of the simulations, it can be assumed that the mesh independence is accomplished. Nevertheless, since the increase in computational cost from one mesh to the other is not too considerable, Mesh 8 is used to perform the rest of the calculations.

Further information about the Mesh independence can be found in Appendix A2.

Convergence criteria (Team 2019; *3 criteria for Assessing CFD Convergence* 2019)

One of the most important and difficult steps to achieve while working with CFD is recognising when the solutions obtained are correct. To do so, it is said that the solution must have converged. Along this project, three main convergence criteria are considered as a reference to validate the results arisen.

- Use of residual values. Residuals directly calculate the error in the solution of the system of equations that is being solved. Given a numerical solution based on an iterative model, this error will never be null. However, it is possible to find values which can be directly approached to 0. Thus, it is considered that when the residuals reach a value around 10^{-3}, the solution is converged.

- Use of solution imbalances. Calculations are made by means of using conservation equations. Therefore, it is necessary that the final solution conserves such parameters. As it happens with the residuals, it is impossible to obtain a null value. However, it is aimed to have an imbalance lower than 1% to assume convergence.

- Use of quantities of interest. This convergence criteria takes into account the number of iterations undertaken and the variation of a certain parameter (forces, force coefficients or moments, amongst others) so that the final value can be considered to be steady.

Evidences of the convergence of the solutions can be found in Appendix A3.

Validation

Once the calculations are made and the data is gathered, it is possible to analyse and offer an overview of the outcomes resultant from the methods applied. In this section, both the results of the CFD simulations and the wind tunnel tests will be presented in an independent manner.

6.1. CFD results

In the CFD study, several parameters were studied with a variation in the boundary conditions and the criteria followed to change them. Thus, two main cases were tackled. The first one implied a variation of the angle of attack while keeping the velocity constant. The most interesting results are obtained from this approach. The second one consisted of a variation of the velocity keeping the angle of attack constant, to see how the different parameters are affected by such velocity variation. The main aim of these simulations is to complement the information acquired for the aerofoil.

6.1.1. Constant velocity

Being able to compare results in both a quantitative and qualitative manner requires the application of the same boundary conditions. Thus, to perform the simulations at a constant velocity, it is decided that a Reynolds number of $1.5 \cdot 10^6$ is used (Ugwueze 2017). By considering sea level conditions and the characteristic dimension to be the chord of the aerofoil, the final result is a velocity of 22.16 m/s, an acceptable value taking into account the flight conditions at which the Lanchester's flight machine will be working (Ugwueze 2017).

To simplify the calculations, the axial and normal forces are calculated, and using equations 3.1 and 3.2, lift and drag are computed. Finally, the forces are converted into their non-dimensional expression and the results can be plotted.

Pressure coefficient distribution

In this section it is going to be analysed the effect that the angle of attack produces on the aerofoil. To do so, the pressure coefficient has been used, in order to express the pressure in a dimensionless way. Figure 14 shows the pressure profiles obtained for different angles of attack.

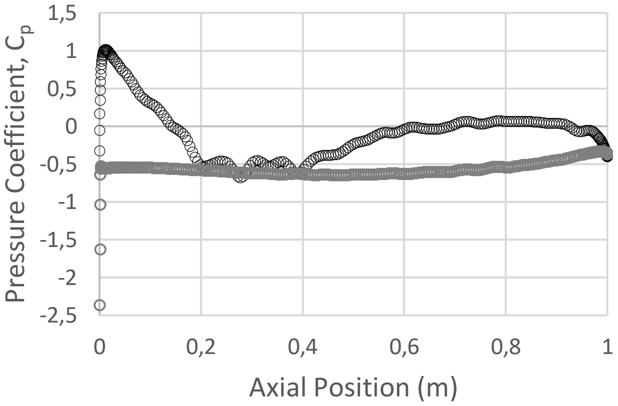

a) α = -10°

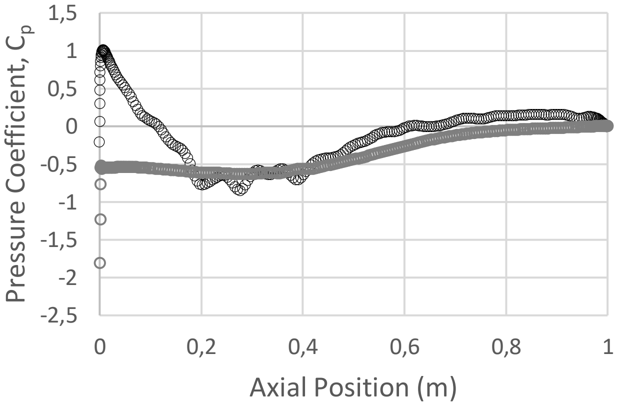

b) α = -5°

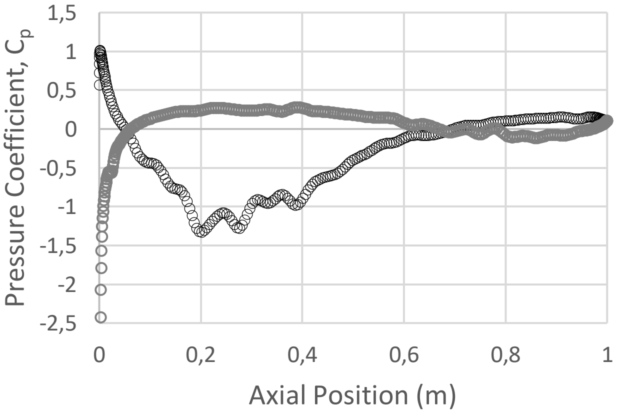

c) α = 0°

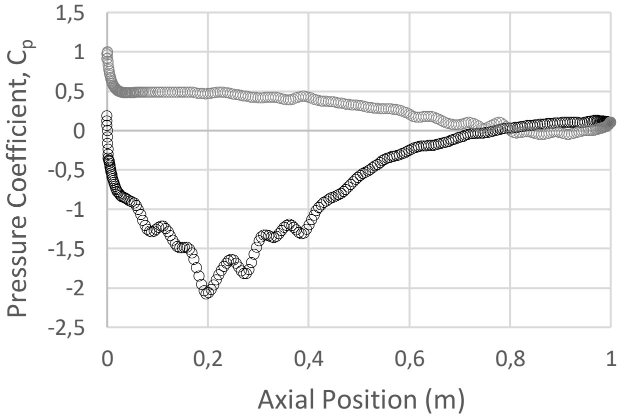

d) α = 5°

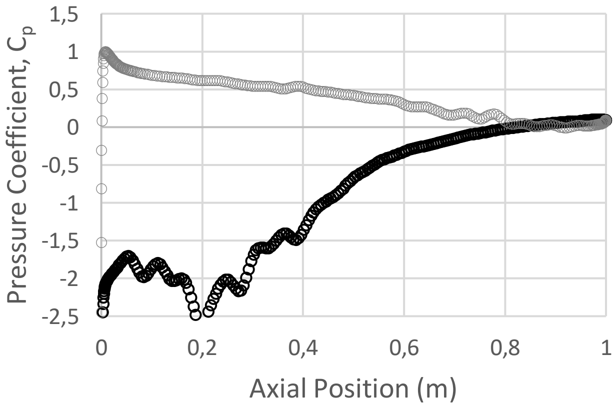

e) α = 8.6°

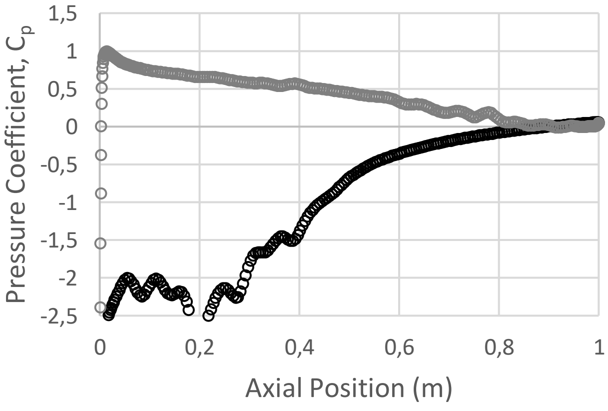

f) α = 10°

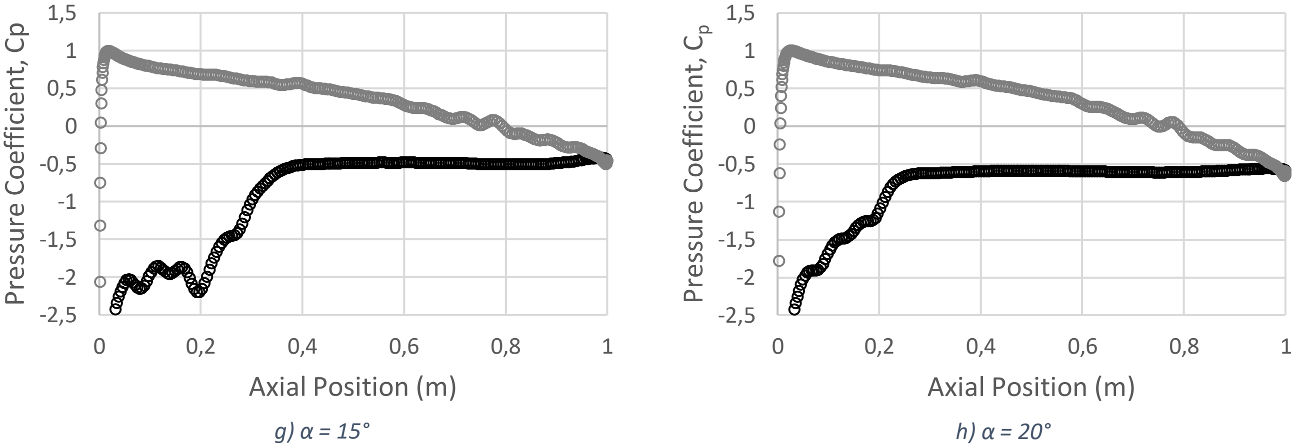

g) α = 15°

h) α = 20°

Figure 14. Pressure coefficient for different angles of attack. (● - grey) intrados. (● - black) extrados.

In order to provide an overview of the evolution of the pressure coefficient, several angles of attack have been analysed, ranging from -10° to 20°, according to the angles analysed while computing the characteristic curves. As a general trend, it can be seen that, as the angle of attack is increased, the area enclosed between the curves representing the pressure coefficient in the extrados and the intrados increases as well, meaning that more lift is being generated.

As it is known, low values for the pressure imply high values of the velocity. Therefore, considering the expression of the pressure coefficient and the reference pressure to be at the sea level, it can be seen that the flow is mainly accelerated in the extrados, since the value for the pressure coefficient is lower (taking negative values).

In the case of plots 14.a and 14.b, representing an angle of attack of -10° and -5°, respectively, a negative value for the lift is obtained. This clearly matches the results obtained with the pressure coefficient, because it is lower in the intrados than in the extrados, causing a downforce instead of a lift force (flow is accelerated more in the lower part of the aerofoil).

Another interesting point to outline is the fact that the greatest variations in the pressure coefficient are seen in the extrados, whereas in the intrados it remains nearly constant independently of the variation of the incident velocity. Also, the most important difference of the pressure coefficient is larger in the leading edge than in the trailing edge. This implies that the lift force generated by the aerofoil is mainly produced in its frontal part.

Finally, the flow detachment can also be observed in the plots provided. If the curve representing the pressure coefficient in the extrados is evaluated, it can be seen that, in the rear part of the aerofoil, it flattens, keeping the value for the pressure constant as it was explained in Section 3.3. This is the representation of the flow detachment. Once the detached flow is present in the major part of the aerofoil, a lift drop is provoked. This flattening occurs when the angle of attack is between 10° and 15°. Therefore, the point at which stall occurs is expected to be between these two values, as it will be seen in the next Section. Also, due to this shape of the extrados' pressure coefficient curve, the area enclosed is lower, supporting the idea suggested at the beginning of the Section.

Lift curve

Simulations have been performed from negative angles of attack up to high positive angles in order to find the point at which stall occurs. All the solutions are considered to be converged, since the criteria established in Section 5.2.1 is accomplished – see Annex A3. The lift curve is characterised by a linear increase of the lift until the critical angle of attack is reached, moment at which a sudden decrease is produced. In Figure 15 the reader can see that this point is located around 10° - although the exact point cannot be provided due to the way Excel treats the experimental data. This seems to be a valid value, since the stalling angle of attack is generally around 15° for most aerofoils (Patel et al. 2014).

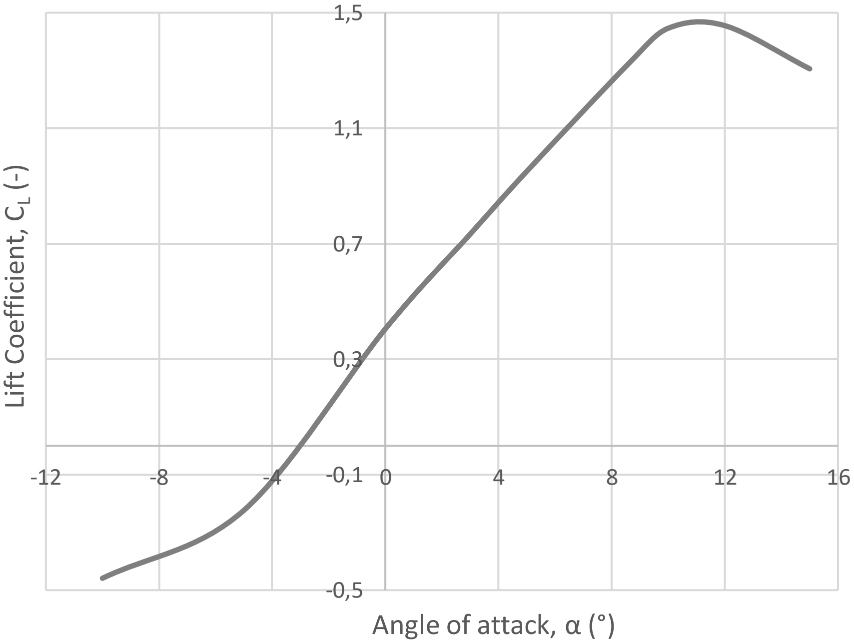

Figure 15. Evolution of the lift coefficient with respect to the angle of attack (CFD).

An interesting point to outline is that the stall in Lanchester's aerofoil does not occur in a hasty way, but it is a moderate decrease. However, it cannot be ignored the fact that CFD calculations do not tend to be precise after stall has occurred, so the results may differ considerably from the real ones. Another interesting point is the effect that the camber produces in the curve. Due to this feature, the aerofoil is capable of generating lift at a null angle of attack. It is possible, therefore, to find the value of the lift coefficient caused by the geometry itself, known as zero angle lift coefficient or CL_0.

$$\mathrm{CL}_0 = 0.4049$$

A further point to analyse while talking about the generation of lift and drag is the velocity and pressure distribution around the aerofoil, as it gives an overview of the flow behaviour. Thus, Figures 20 to 29 show the velocity and pressure profiles of the flow around the aerofoil at some of the angles of attack that have been studied and an explanation of their influence is provided.

Drag curve

As expected, the equation defining the drag generated by the aerofoil is quadratic. It is complicated to determine the drag produced by an aerofoil under stall conditions, although an approach is provided (*Inclination effects on Drag* 2019). The data obtained – available in Appendix A5 – proves that the lowest drag will be produced at a null angle of attack, although due to the data treatment in Figure 16 it seems to be at an angle of attack of 1°. The reason for such behaviour is that, the more the angle of attack is increased, the greater is the force generated in the direction tangential to the flow and, consequently, lower in the normal one.

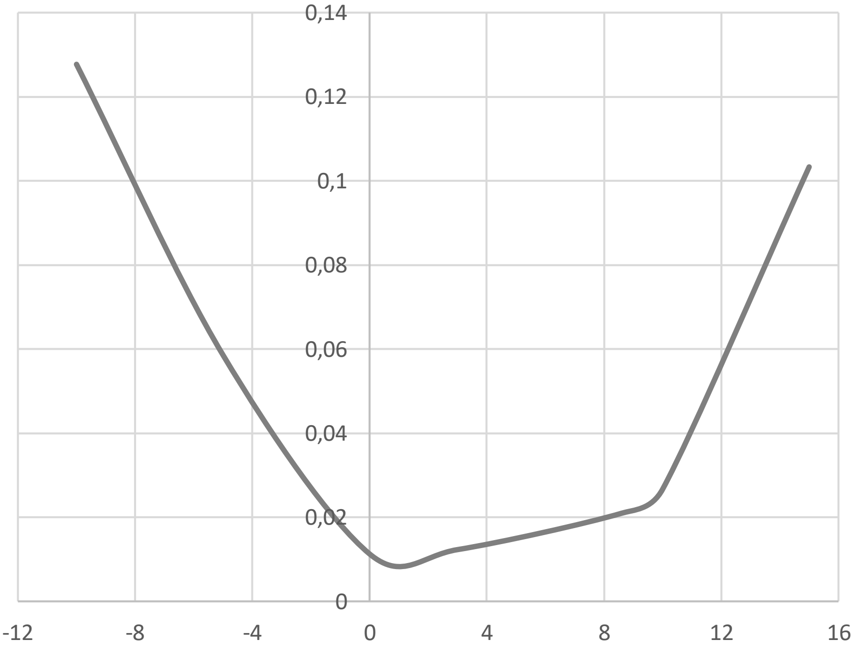

Figure 16. Evolution of the drag coefficient with respect to the angle of attack (CFD).

Drag polar curve

Once the values for both the lift and the drag are calculated, it is possible to elaborate the drag polar curve, which relates the variation of the drag coefficient with respect to the increment of the lift coefficient. As a consequence of the existence of a relationship between lift and drag, it is also possible to find the zero lift drag coefficient or CD_0, which is the value for the drag coefficient at which no lift is being generated. Also, the value for the minimum drag coefficient can be obtained:

$$\mathrm{CD}_0 \approx 0.04$$

$$\mathrm{CD}_{\mathrm{min}} = 0.0112$$

Moreover, this plot depicts the aerofoil performance under given conditions. Thus, it allows to get the value for the maximum aerodynamic efficiency, which is defined as the lift-to-drag ratio and is one of the most important factors to consider in aircraft design. In Figure 17 the graphical obtaining of the aerodynamic efficiency is shown together with the drag polar, whereas Figure 18 represents the variation of the aerodynamic efficiency with respect to the angle of attack.

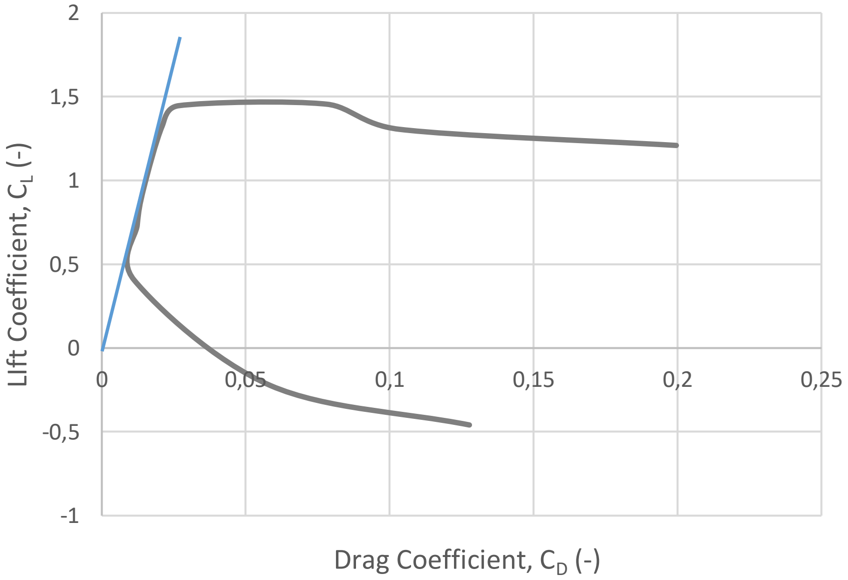

Figure 17. Evolution of the lift coefficient with respect to the drag coefficient (CFD).

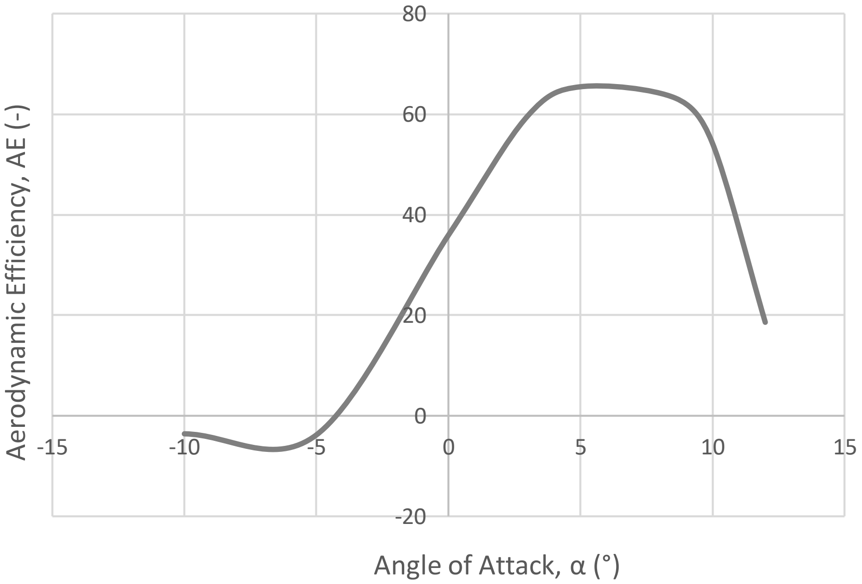

Figure 18.Evolution of the aerodynamic efficiency with respect to the angle of attack (CFD).

Another further point to comment is the evolution of the drag coefficient with respect to the aerodynamic efficiency. As it can be seen in Figure 19, it presents a decreasing trend, implying that the higher the quotient between lift and drag, then the lower the value of the drag coefficient.

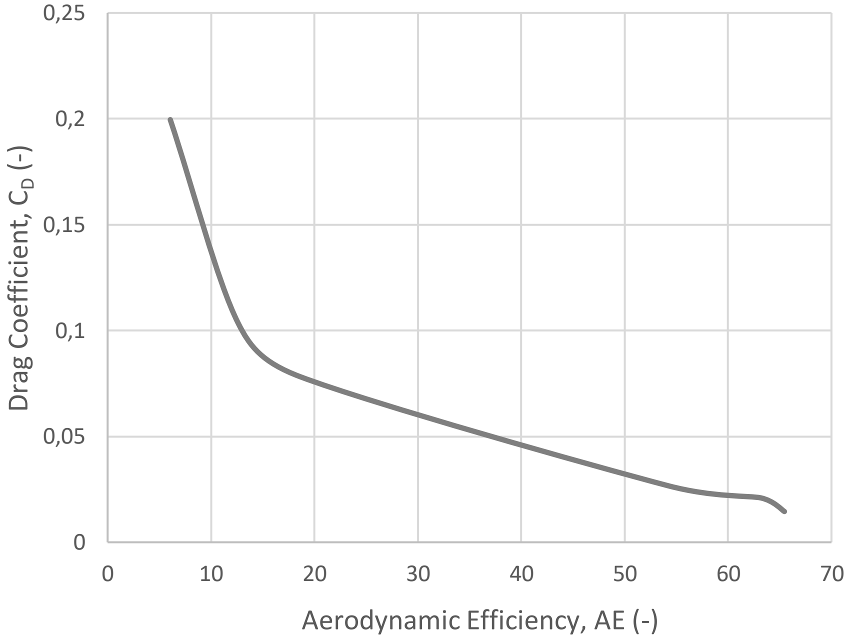

Figure 19. Evolution of the drag coefficient with respect to the aerodynamic efficiency (CFD).

Finally, the reader must not lose sight of the fact that these results are being computed at a 2D case, considering the aerofoil as an infinite element and ignoring the 3D effects of the wing. In the case of a 3D wing, these values may be reduced, due to the interfering factors resulting from such treatment.

Next, as it has been stated, the graphical results obtained with StarCCM+ will be presented. They offer a visual approach to the numerical results that have been explained, showing which the implications of the velocity and static pressure distributions are.

Angle of attack α = 0°

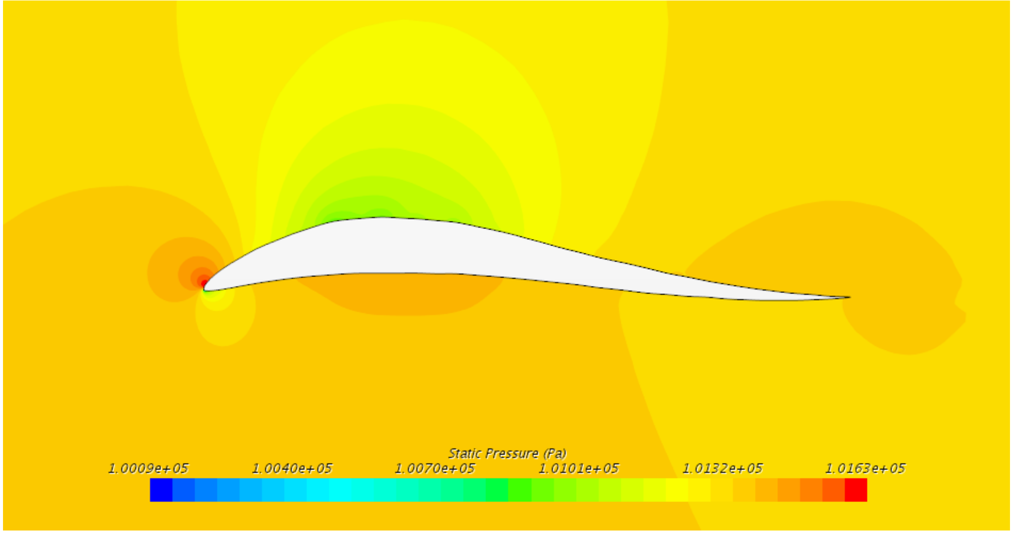

Figure 20. Static pressure contour for an angle of attack α = 0°.

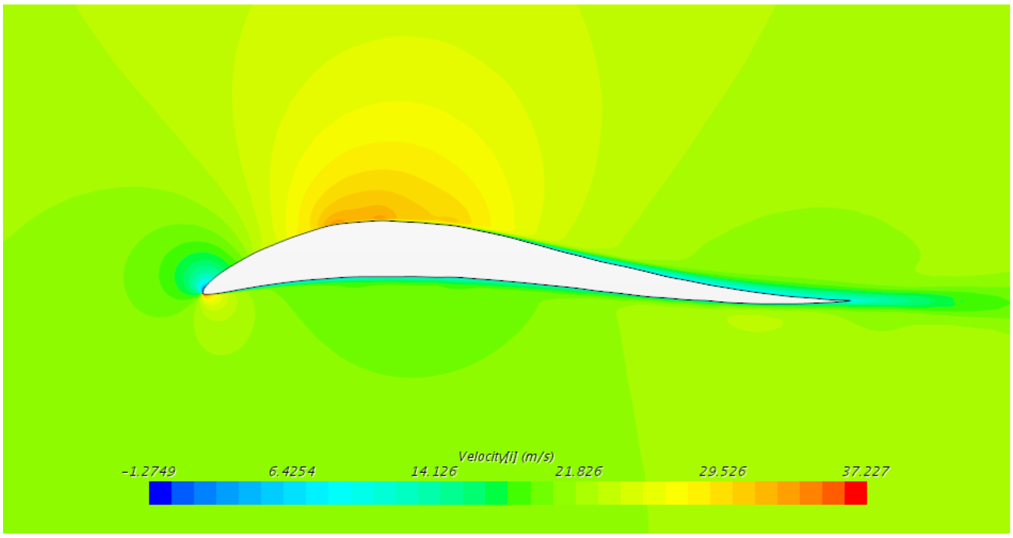

Figure 21. Velocity contour for an angle of attack α = 0°.

For a null angle of attack, there is a great difference in the value of the static pressure in the extrados and the intrados. It can be seen that there is an increase in the intrados, whereas its value in the extrados is now lower. This contributes to the generation of lift. Since the pressure difference between both surfaces is greater, then the value of the force generated will be higher.

From the velocity contour, it can be seen that there is an acceleration of the flow in the extrados, in the part where the thickness of the aerofoil is maximum. Towards the trailing edge, there is a deceleration of the flow, as well as a stagnation point (region with low velocity and high pressure) located in the leading edge.

This position of the aerofoil is the one creating less drag. This is due to the fact that it is the position at which the aerofoil presents a lower surface interfering the flow and, therefore, it adapts in a more subtle and less sharped manner.

Angle of attack α = 5°

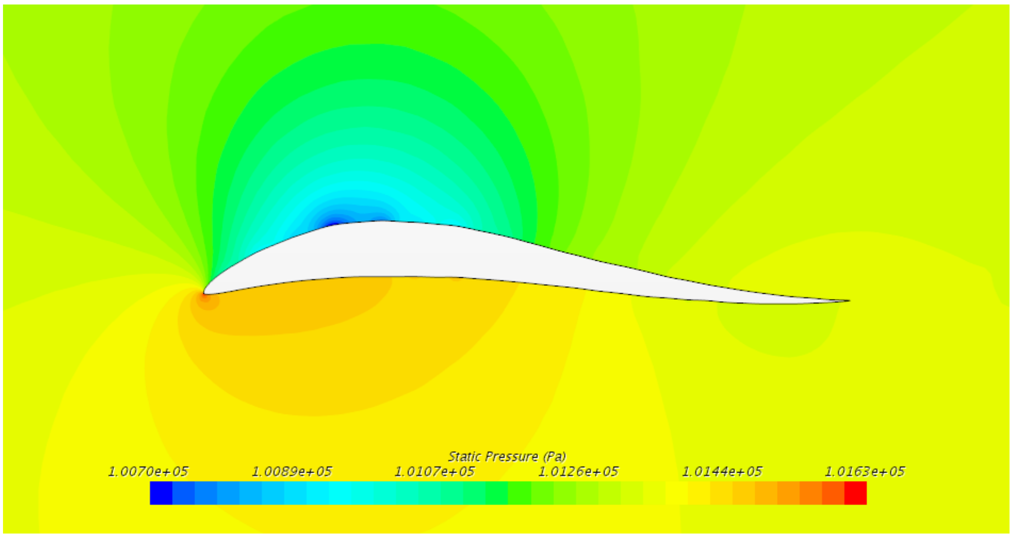

Figure 22. Static pressure contour for an angle of attack α = 5°.

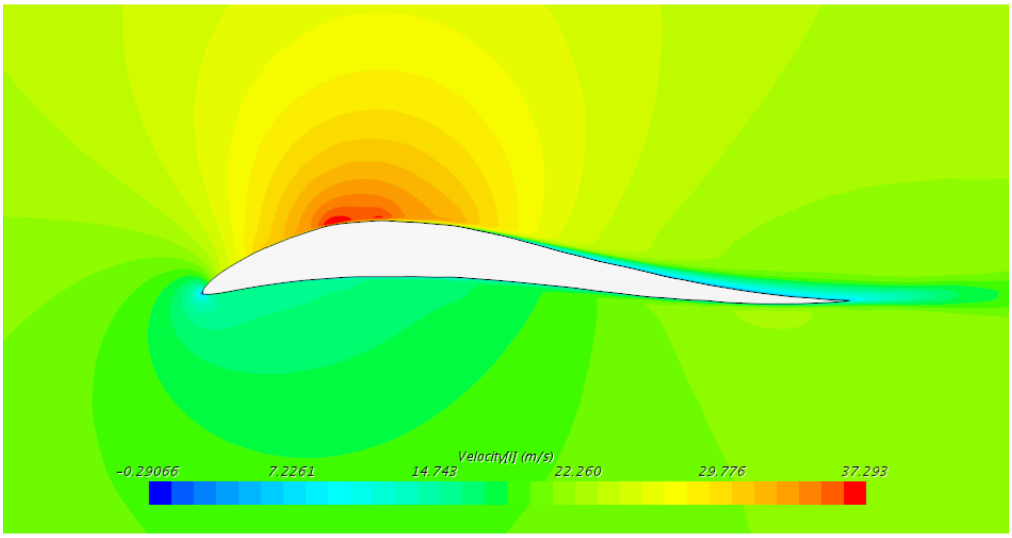

Figure 23. Velocity contour for an angle of attack α = 5°.

For an angle of attack of 5°, Figure 22 shows that the flow has a stagnation point at the leading edge, causing an increase of the lift force in the upwards direction. Also, the value for the pressure is generally higher in the intrados, causing a deceleration of the flow and therefore supporting the generation of such force.

In terms of the velocity contour, Figure 23 shows that a deceleration appears towards the trailing edge of the aerofoil, mainly in the area after the main curvature is located. Relating this contour to the static pressure one, it can be seen that the stagnation point can be now associated to a region at which there is a decrease in the oncoming velocity, reaching a null value at the point of maximum pressure.

Angle of attack α = 10°

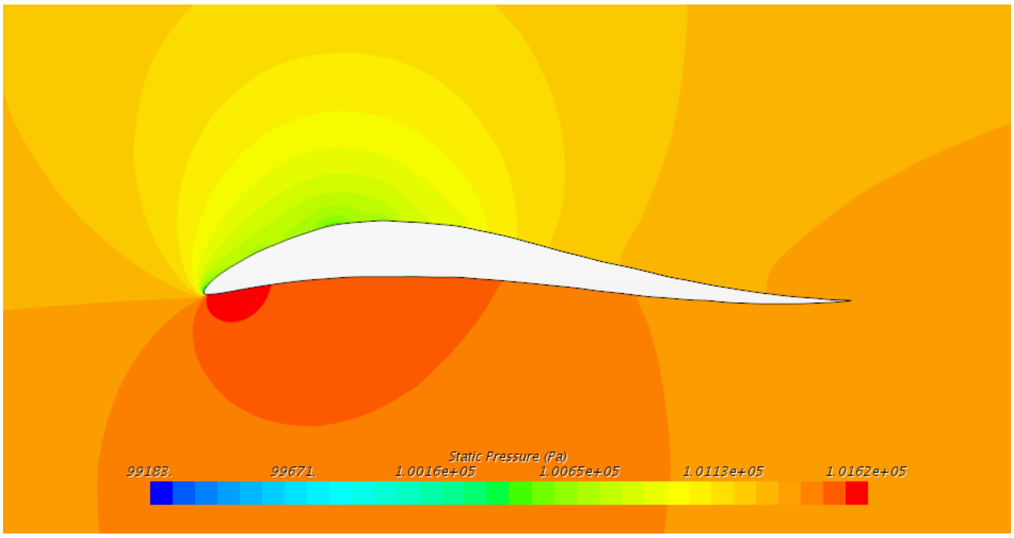

Figure 24. Static pressure contour for an angle of attack α = 10°.

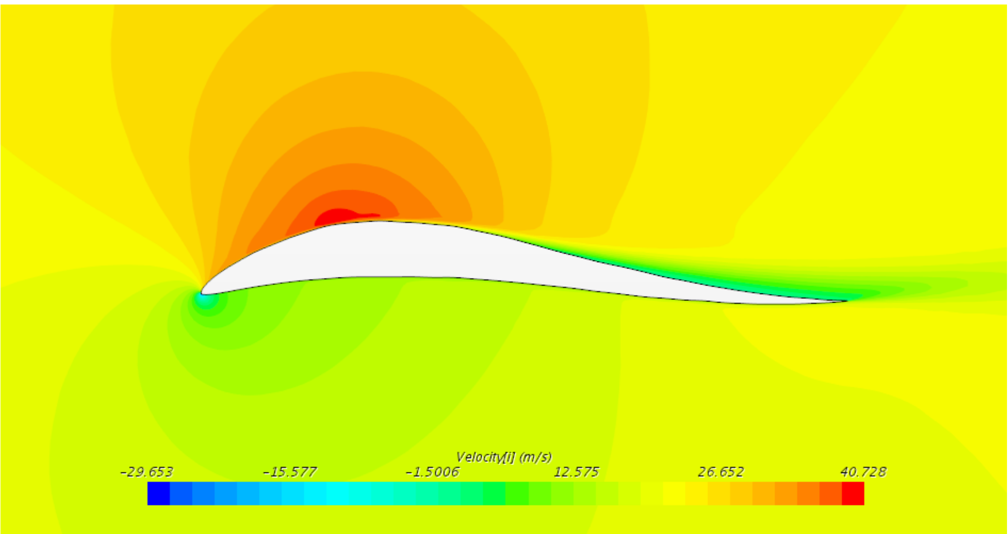

Figure 25. Velocity contour for an angle of attack α = 10°.

In the case of applying 10° for the angle of attack, the stagnation point has been displaced below the leading edge, creating a force upwards and giving as a result the positive lift. As it happened at an angle of attack of 0°, the pressure difference between extrados and intrados has increased, augmenting the value for the lift.

In terms of the velocity, there is an acceleration in the upper surface of the aerofoil, whereas there is a deceleration in the lower part. There are minor changes related to the behaviour of the flow with respect to the previous case, except for the fact that both the acceleration and deceleration of the flow are more noticeable in this case.

Increasing the angle of attack implies increasing the contact surface as well. Thus, even when the drag coefficient is kept nearly constant at low angles of attack, 10 degrees are a considerably high value – even though the detachment of the boundary layer is not too important. Therefore, a higher value for the drag coefficient is expected.

Angle of attack α = 15°

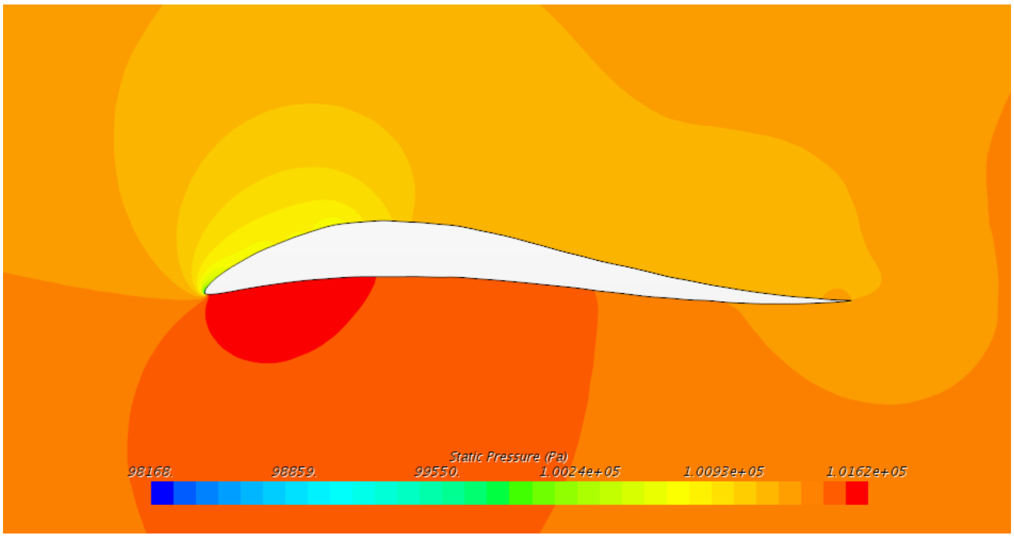

Figure 26. Static pressure contour for an angle of attack α = 15°.

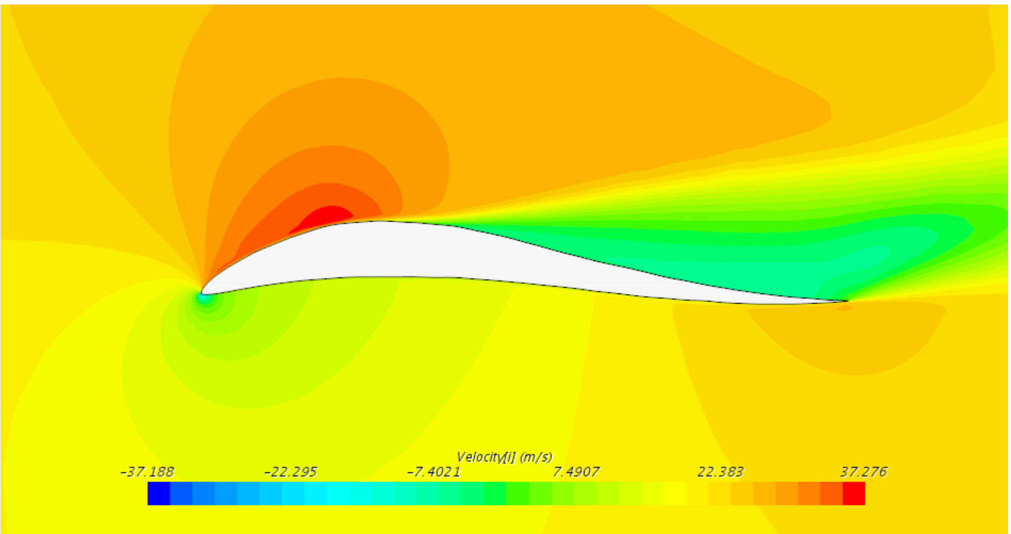

Figure 27. Velocity contour for an angle of attack α = 15°.

In the case of an angle of attack of 15°, the area of highest pressure has expanded, diminishing the pressure difference between both surfaces of the aerofoil and therefore justifying the decrease in lift shown in Figure 15. Due to this high pressure difference, the major contribution for the lift is performed in the front part of the aerofoil.

In Figure 27, the velocity contour can be analysed. The wake of the aerofoil presents null values for the velocity. In this way, there is a reduction of the lift force due to the boundary layer detachment. It is complicated to determine the drag produced by an aerofoil under stall conditions, although an approach is provided.

Angle of attack α = 20°

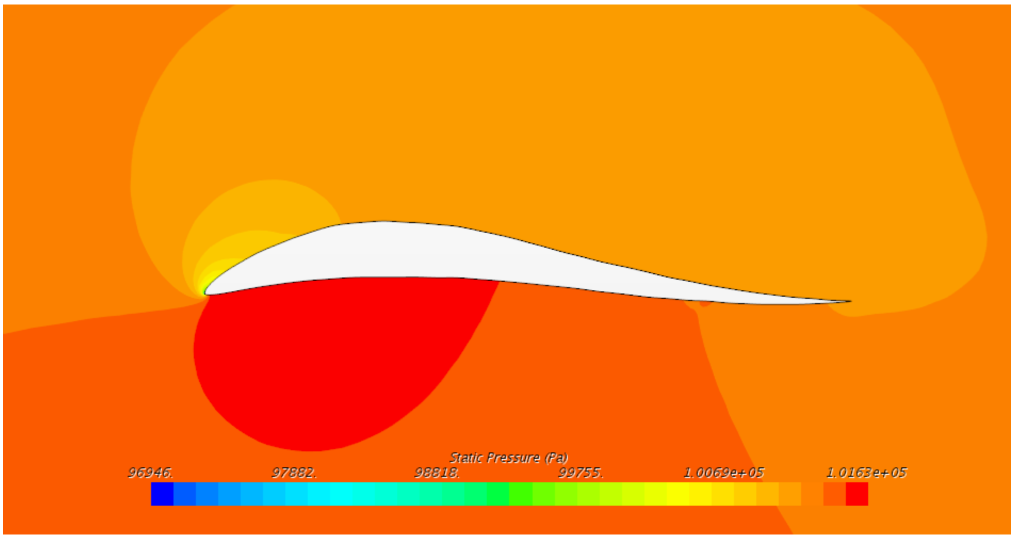

Figure 28. Static pressure contour for an angle of attack α = 20°.

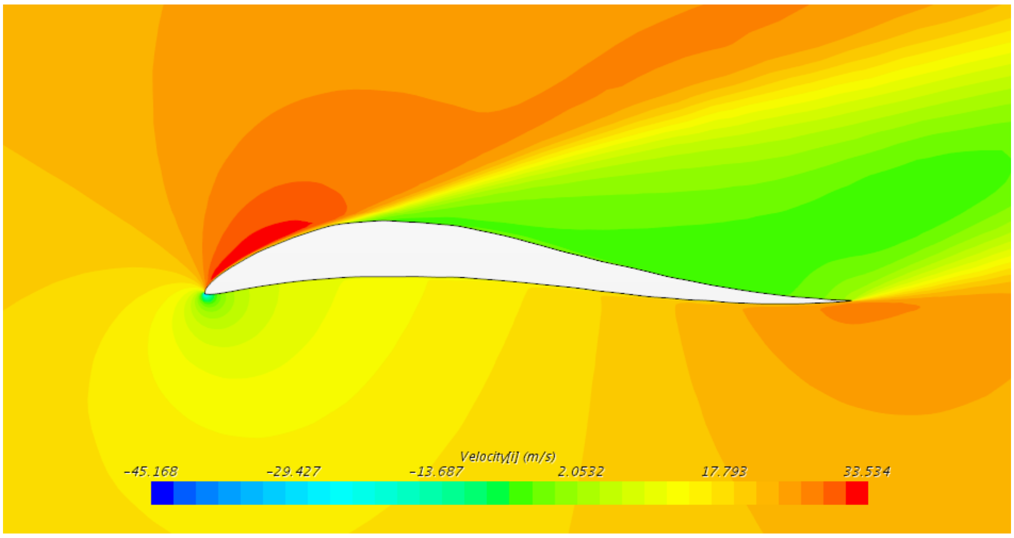

Figure 29. Velocity contour for an angle of attack α = 20°.

Finally, for the highest angle of attack that has been applied, it can be seen that all the main features described for the previous case have been magnified.

In the case of the pressure, higher values are to be found both in the extrados and the intrados, although the overall pressure difference is lower. This justifies the decrease in lift coefficient characterising the stall.

As for the velocity, the region at which a null velocity is created has been expanded, provoking a bigger wake and therefore working against the lift.

In these last two cases, where the boundary layer is clearly detached and the flow presents eddies and recirculation, drag is difficult to calculate, since its behaviour is not defined after stall. Nevertheless, it is known to be growing, both due to the flow behaviour towards the trailing edge – pressure drag is increased when the boundary layer detaches – and the increase of the surface opposed to it.

A point to highlight from all the scenes presented in this sections is that the pressure and velocity before the leading edge and after the trailing edge must correspond to the values determined in the boundary conditions – the velocity from the inlet and the pressure from the outlet, respectively. Nevertheless, as it has been seen, this recovery to the free-stream conditions does not occur immediately, but it needs a certain transition area.

As a summary, it can be stated that the curves obtained for the lift and drag coefficients (Figures 15 and 16 respectively) perfectly match the reasoning and results arisen while considering the velocity and pressure contours.

6.1.2. Constant angle of attack

As a way of expanding the study of Lanchester's aerofoil, the second set of simulations consists on the variation of the velocity – and therefore the Reynolds number – keeping the angle of attack constant. By doing so, it is possible to see how does the drag evolve with respect to the velocity and prove its quadratic tendency. If it was possible to separate the components of the drag coefficient – parasitic and induced drag – it would be possible to observe that the low speeds are governed by the parasitic drag whereas the high ones are regulated by the induced drag.

As it was explained in Section 5.1, compressibility effects arise when the Mach number is higher than 0.3. Considering the atmospheric and gas conditions that are being assumed, this Mach number corresponds to a velocity of 100m/s. Therefore, to simplify the calculations and just as a complementation of the information shown above, the low speeds will be simulated in order to prove the quadratic behaviour followed by the drag coefficient.

As it was stated, the drag force, and as a result the drag coefficient, at low speeds is regulated by a quadratic function due to the effects of the induced drag. As the value of the velocity increases, this type of drag is reduced and the effects of the pressure drag start increasing.

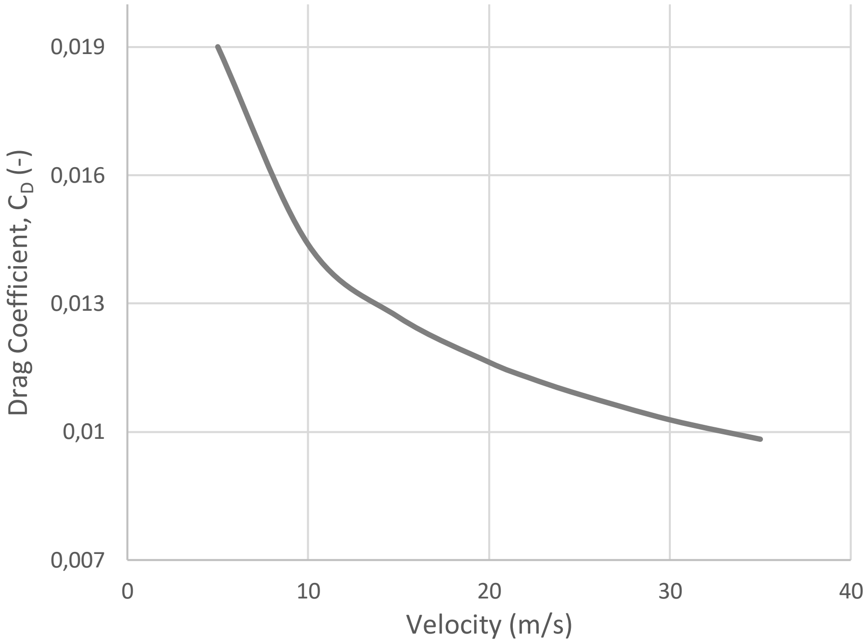

Figure 30. Evolution of the drag coefficient with respect to the velocity (CFD).

6.2. Wind tunnel results

The same results were pursued while performing the wind tunnel measurements. Nevertheless, due to structural limitations, there were variations with respect to the expected results.

The first and most important difference is the velocity at which the experiment has to be performed. According to the Reynolds number conservation and attending the scale factor of the model, the velocity in the wind tunnel should be 10 times the velocity used in the simulations – see Appendix A4. Attending to the value used for all the simulations, this would imply reaching velocities between 50 and 350 m/s. As expected, these velocities could not be achieved in the wind tunnel, reason why they were done without considering the scale factor applied. Ignoring that condition means working in a different flow regime (laminar instead of turbulent) what leads to difference in the results that have been obtained.

The second difference is the pitching angle that the aerofoil will be experiencing. The highest pitching angle available with the actuator is 18°, slightly different to the ones that have been used in the simulations. The main implication is that it will not be possible to compare the results at high angles of attack. Also, in terms of negative angles of attack, the structure could not stand the minimum of -10°, so the experiment was finished when applying an angle of attack of -5°.

6.2.1. Constant velocity

In this first experiment, a constant velocity of 22 m/s has been applied, trying to maintain the experiment as relatable as possible to the simulations.

Lift curve

Measurements have been performed in intervals of 5°. Figure 31 shows the clear tendency that characterises the lift curve, having a linear increase at low angles of attack up to an angle around 16° at which it suffers a sudden decrease. This angle of attack corresponds to the stall angle of attack. Once this point is reached, the behaviour of the flow is more difficult to analyse, since it does not follow a certain pattern.

At this point it is possible to calculate the zero angle lift coefficient:

$$\mathrm{CL}_0 = 0.311$$

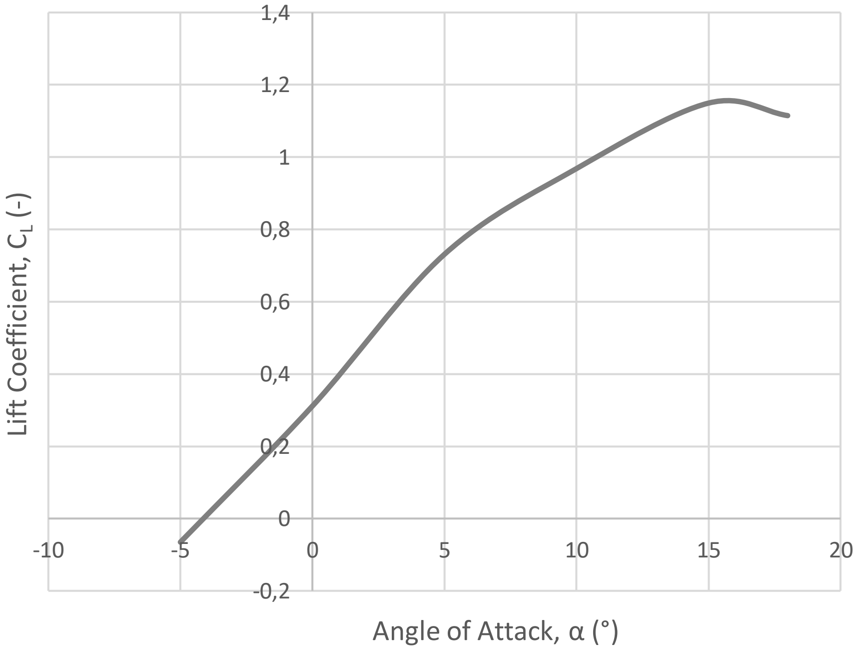

Figure 31. Evolution of the lift coefficient with respect to the angle of attack (Wind Tunnel).

Drag curve

The drag curve presents a quadratic trend, having its minimum value at a null angle of attack – again this statement is deduced from the data obtained from the wind tunnel, not the Excel treatment.

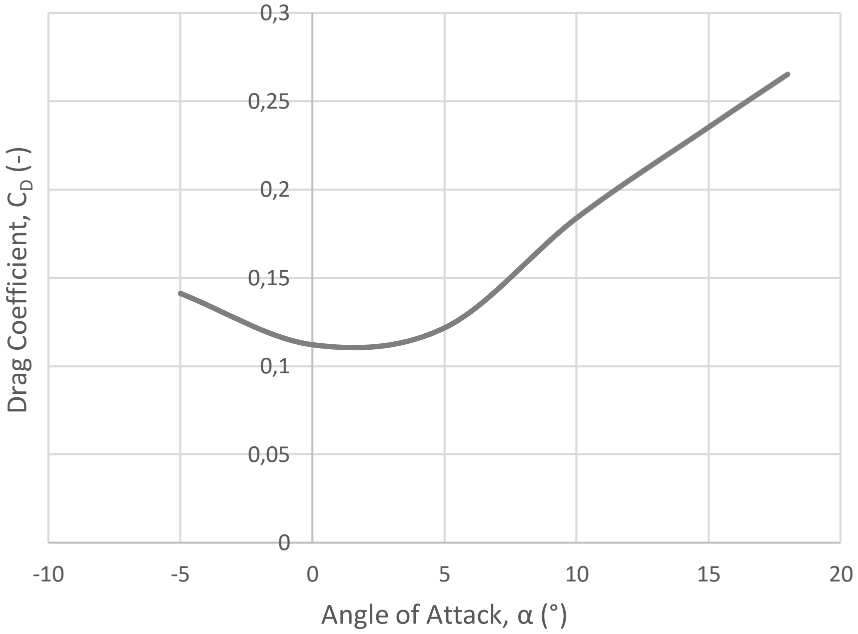

Figure 32. Evolution of the drag coefficient with respect to the angle of attack (Wind Tunnel).

Drag polar curve

Once the values for both the lift and the drag are calculated, it is possible to elaborate the drag polar curve. Again, it is easy to calculate the values for the CD_{min} and CD_0:

$$\mathrm{CD}_0 \approx 0.14$$

$$\mathrm{CD}_{\mathrm{min}} = 0.112$$

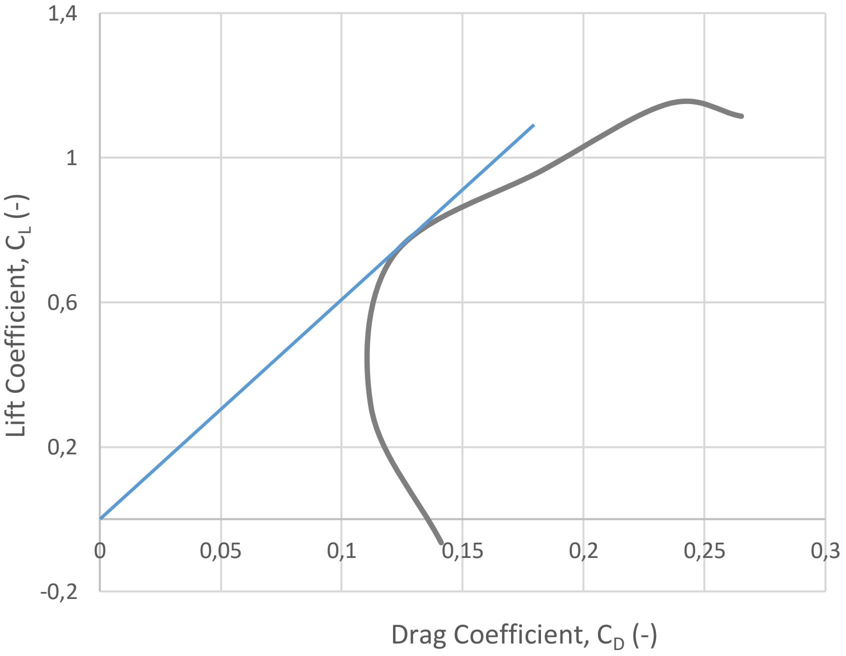

Figure 33. Evolution of the lift coefficient with respect to the drag coefficient (Wind Tunnel).

By applying the graphical method to calculate the maximum aerodynamic efficiency of the wing, Figure 34 shows that its maximum value is reached at the drag coefficient value corresponding to an angle of attack of 6°, approximately.

It is also possible to analyse the evolution of the aerodynamic efficiency with respect to the angle of attack in order to support the ideas that have just been exposed.

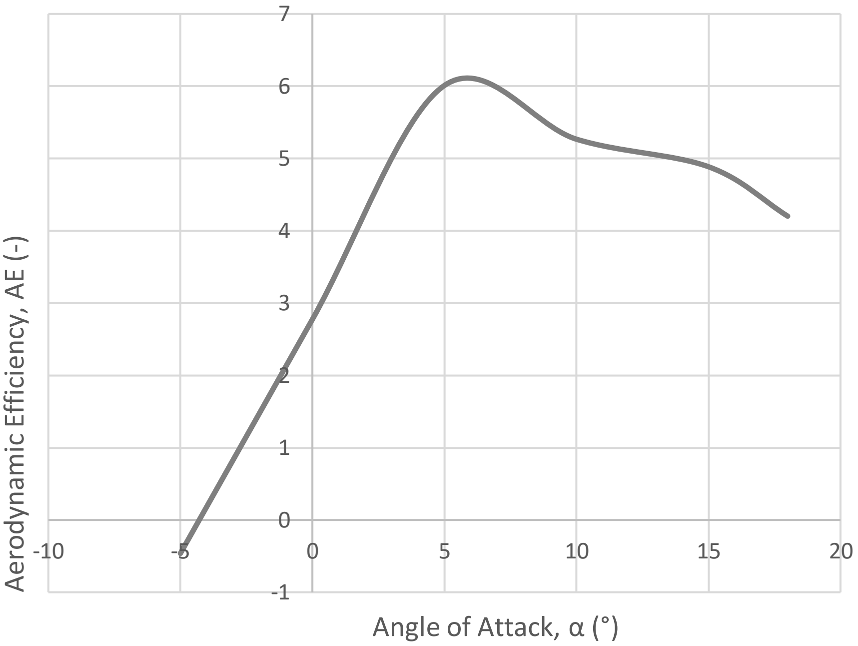

Figure 34. Evolution of the aerodynamic efficiency with respect to the angle of attack (Wind Tunnel).

In Figures 34 it can be seen that it supports the ideas that were exposed for the rest of the parameters studied. In the same line, the aerodynamic efficiency presents an increasing trend from the negative values of attack up to its maximum, located at 6°. Afterwards, it starts descending, meaning that the lift-to-drag ratio is reduced.

6.2.2. Constant angle of attack

In this case, again 6 experiments have been undertaken, varying the velocity from 10 m/s up to 35 m/s. Since the structure could not withstand higher values of the velocity, again, only low velocities – low Reynolds numbers – are being analysed.

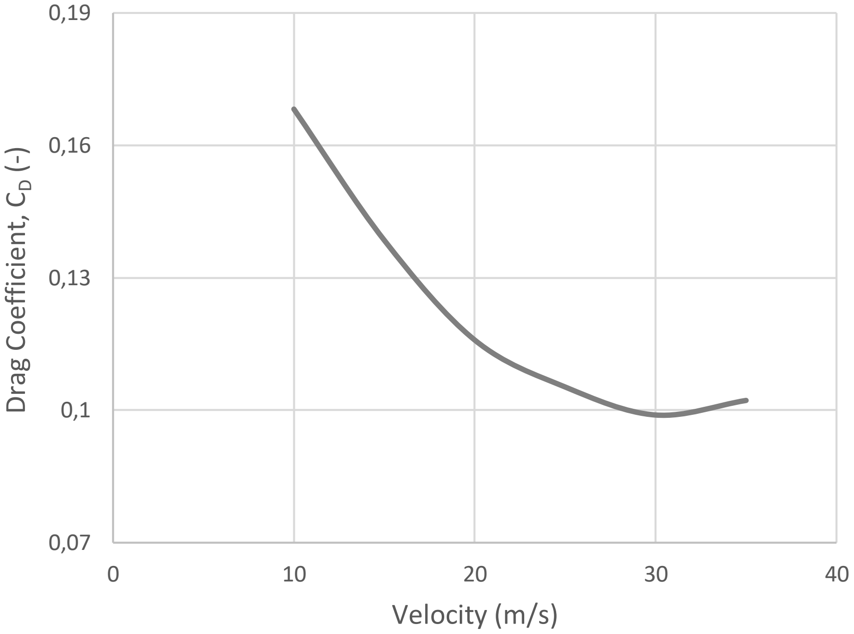

Figure 35. Evolution of the drag coefficient with respect to the velocity (Wind Tunnel).

Again, the tendency corresponds perfectly to the theory. An interesting point to outline is that at 35 m/s there is an increase in the value of the drag coefficient. This could represent the starting point of the right hand branch governed by the lift-induced drag. However, due to structural limitations, this statement cannot be proved and will be left for further studies of the LAN1897 aerofoil.

Comparison of the results

In the previous chapter, the results obtained for the wind tunnel and the CFD simulations were presented independently. Next, this chapter shall analyse the results comparing their trends and outlining their discrepancies and similarities from an aerodynamic point of view. It must be remarked that values cannot be directly compared, since results are obtained from a 3D and a 2D approach, respectively. Therefore, three-dimensional effects will arise as seen in Section 3.4. Nevertheless, it is possible to offer an overview on the similarities, discrepancies and effects between both considerations.

7.1. Lift curve

In aeronautical terms, the difference between an aerofoil and a finite wing is the aspect ratio. An aerofoil is a wing with infinite aspect ratio, whereas a wing has a finite value for such parameter.

If the lift coefficient for both elements is plotted with respect to the angle of attack, it can be seen in Figure 36 that the aerofoil has a greater maximum lift coefficient, although its critical angle of attack is lower.

The difference in the maximum lift coefficient is justified by the appearance of the wingtip vortices in the 3D case. When considering a finite span, the wing enables the air flowing into the region of low pressure. In that way, the overall pressure differential is reduced and, as a consequence, the overall lift is reduced as well.

In the case of the difference of the stall angle of attack, it is produced due to the airflow in the extrados of the wing. This airflow provides energy to the air – and as a consequence, to the boundary layer –, reason why it is called as re-energisation. This re-energisation increases the velocity in the upper part of the aerofoil, keeping the boundary attached to the surface for a longer time. Consequently, if the boundary layer remains attached, the tendency for the airflow to separate is reduced and the wing does not stall.

As a consequence of all the arguments stated above, the slope of the lift curve from the finite wing is reduced.

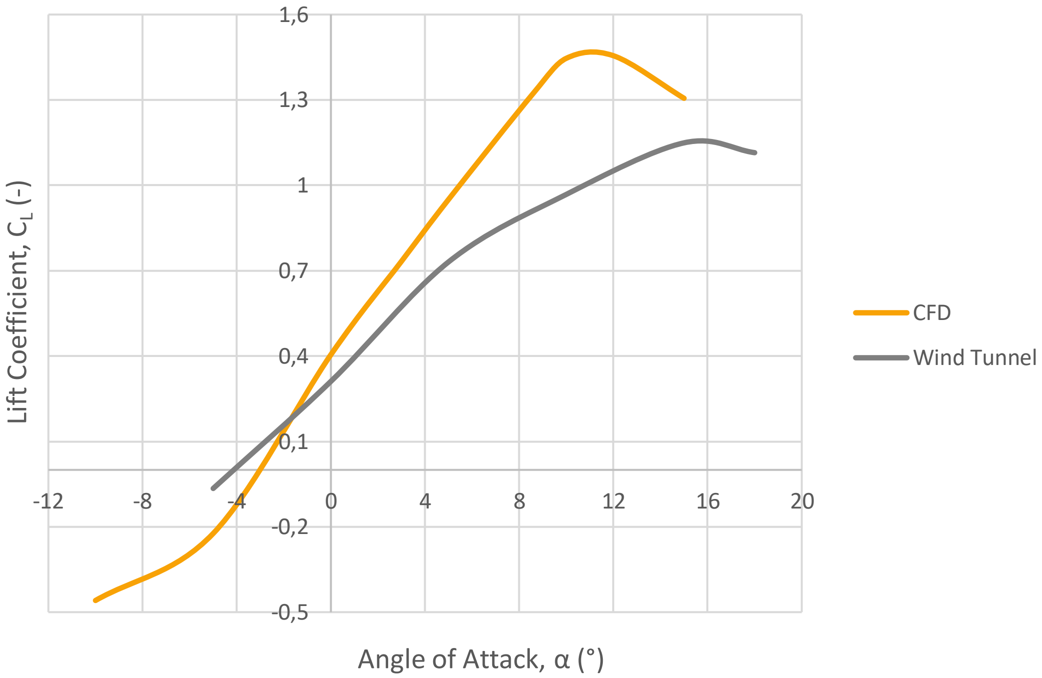

Figure 36. Lift coefficient curve comparison.

7.2. Drag curve

Significant differences can also be found regarding the drag coefficient in aerofoils and finite wings. Figure 37 shows that the value for the drag coefficient is generally higher in the case of the finite wing. This is mainly due by the fact that there are interfering factors in the wind tunnel whose influence affects the final result for the drag. These factors are the attachments, the rod, the glue and the tape used to fix the structure, which changes the surface roughness and causes the airflow to disturb.

Another of the differences between an aerofoil and a finite wing is that, the latter one is capable of generating lift induced drag as a result of the existence of the wing tip vortices. Thus, since a further component is acting on the drag generation, higher values are expected, as seen in Figure 37.

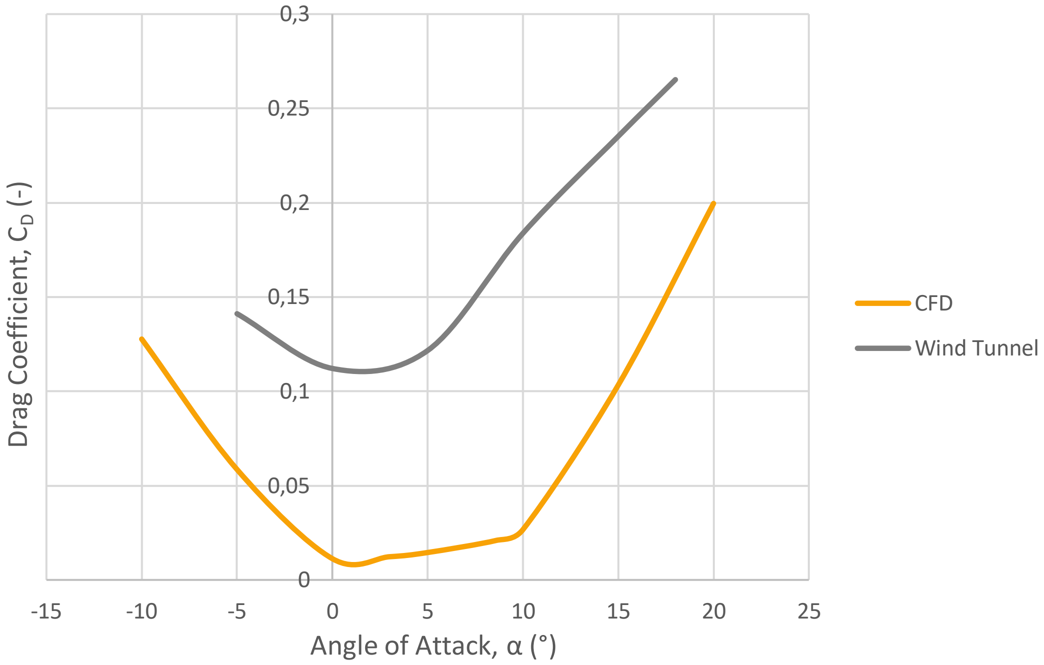

Figure 37. Drag coefficient curve comparison.

7.3. Drag polar curve

If the drag polar curves are compared, it can be seen in Figure 38 that the CFD approach curve is displaced towards the left with respect to the wind tunnel results and also reaches higher values for the lift coefficient.

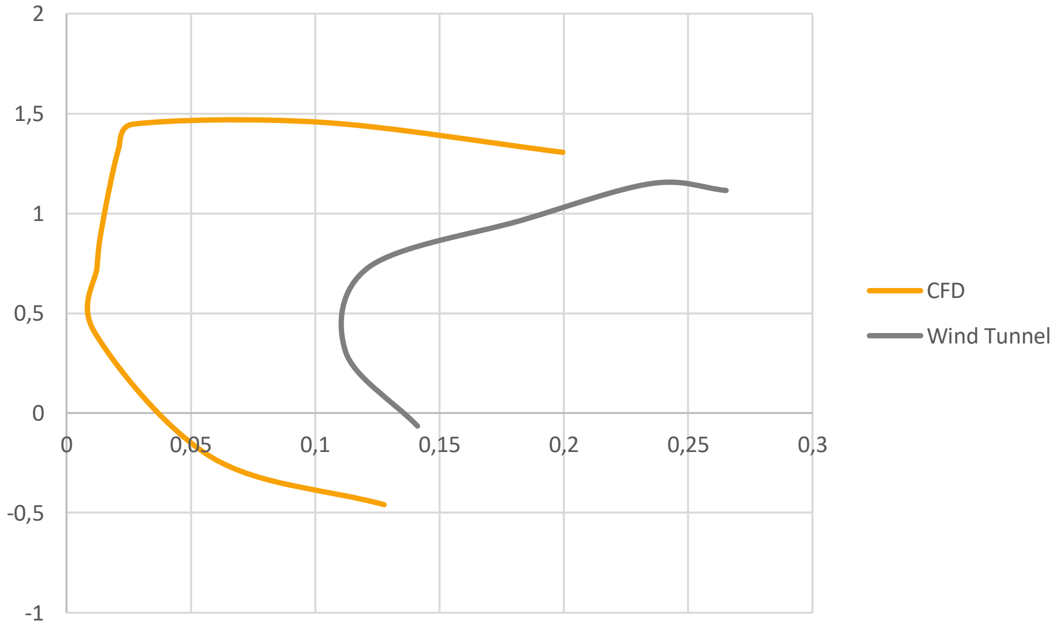

Figure 38. Polar drag curve comparison.

If the two previous graphs are considered (Figures 36 and 37), this result perfectly matches the expected behaviour, because the finite wing creates a higher value for the drag – justifying the displacement towards the right – whereas the aerofoil is capable of generating higher lift – reason why the CFD curve is wider.

7.4. Aerodynamic Efficiency

Finally, it was stated in Section 6.1.1 that the 2D approach would offer higher values for the aerodynamic efficiency than the finite wing. In this Section, this affirmation will be proved. If the reader focuses on Figure 39, it can be seen that the finite wing's efficiency is around 10 times smaller than the one obtained for the aerofoil.

Considering the comparisons made in terms of the lift and the drag, lift for the aerofoil is higher whereas drag is lower. Next, knowing that the aerodynamic efficiency is calculated as the quotient between these two parameters, it is easy to deduce that aerofoils will offer higher ratios of aerodynamic efficiency than finite wings.

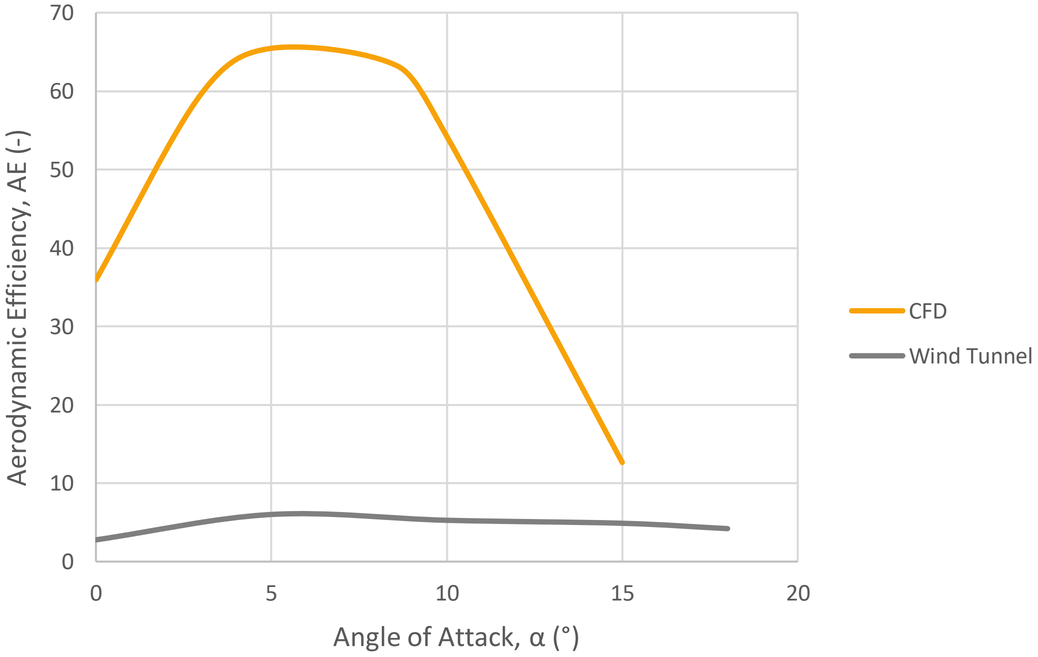

Figure 39. Aerodynamic efficiency comparison.

In Figure 40, a secondary vertical axis has been added so that a comparison of the trend can be undertaken. Thus, the analysis for the aerodynamic efficiency of the finite wing must be performed taking into account such secondary axis.

For both approaches, the tendency for low angles of attack is the same, an increasing tendency of the aerodynamic efficiency caused by the noticeable increment of the lift coefficient (Figure 36) together with a negligible increment of the drag coefficient (Figure 37).

Even if the value for the aerodynamic efficiency for the aerofoil flattens around a value of 65, it reaches its maximum approximately at the same angle of attack as the finite wing – approximately 6°. This is a further evidence that both approaches offer similar results in terms of the qualitative analysis. Finally, right after the maximum value has been reached, both the aerofoil and the finite wing provoke a decrease in the aerodynamic efficiency, being the one of the wing more subtle. This could be explained knowing that force coefficient and flow behaviour is difficult to analyse after stall conditions, and the aerofoil enters stall at lower angles of attack than the finite wing, as seen in Figure 36.

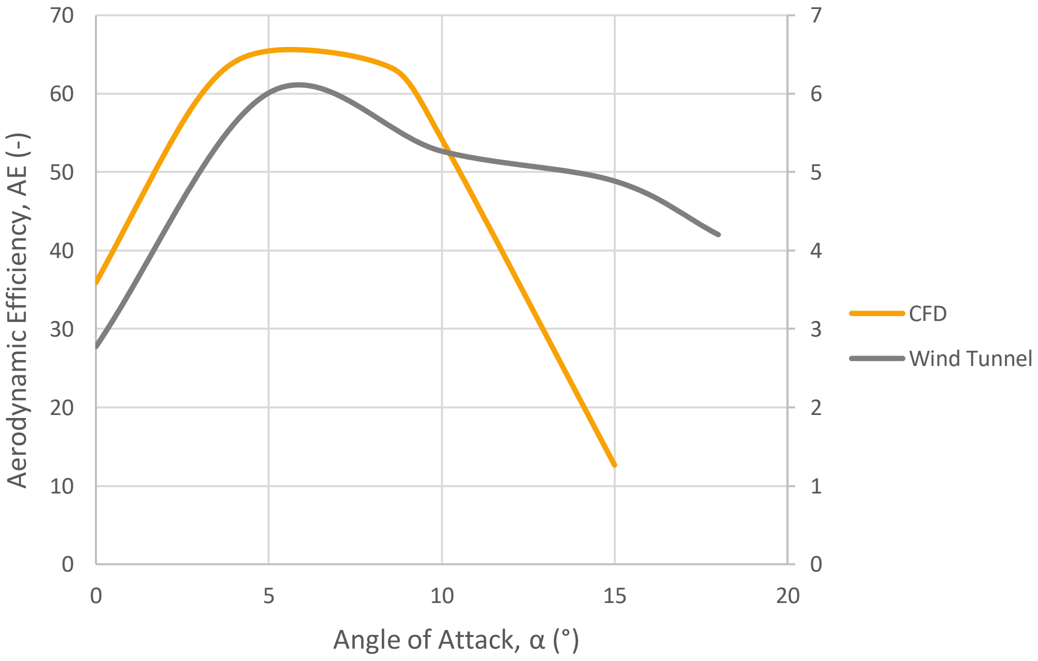

Figure 40. Aerodynamic efficiency comparison (detail).

Conclusions

Along this dissertation, all the stages of the CFD process and experimental method have been tackled. Consequently, several conclusions have been drawn, regarding both the results obtained and the methods and procedures applied.

In terms of the procedures that have been undertaken, by performing the CFD pre-process it has been made clear the importance of a good mesh quality. Carrying out a good CFD analysis requires the development of a proper mesh independence, altogether with the selection of the appropriate parameters that will give the correct results. At this point, the mesh typology, the stretching applied and the density of cells will play a key role. Also, the computational cost must not be ignored, as a relationship between refinement and time must be created.

Moreover, considering the manufacturing process, the use of the 3D printers has been decisive. In the recent years, light materials have started to conquer the market. Thanks to the cheap cost of such materials and the easiness of their use, they entail a great advantage for experimental procedures, offering both students and technicians a good alternative to more traditional materials such as foam.

Regarding the general performance of the aerofoil, it is possible to affirm that it offers good capabilities for sustained flight. If the values calculated for all the parameters studied along the parameters are compared with the ones of the most popular aerofoils in the market, it can be stated that the LAN1897 offers a good alternative at low Reynolds numbers and subsonic flow. Said so, it is remarkable and admirable the fact that, back in the 19th century and with the complete aerofoil theory being developed in the meantime, Lanchester was able to develop an aerofoil with these capabilities.

By comparing the results obtained by means of the two methods developed in this project altogether with the ones present in previous bibliography (Ugwueze 2017), it is possible to see that the variations that have emerged are not too significant. In fact, such discrepancies could be considered to be an effect from the use of a different Software and approach. While XFoil is a simulating tool englobing general parameters of aeronautics: aerodynamics and flight mechanics, amongst others, StarCCM+ offers a more robust tool is terms of flow behaviour considerations. Thus, looking at the variations that appear the results can be considered to be lawful and valid.

Finally, as for the results obtained from the 2D and 3D consideration, it has been possible to see the differences in behaviour that they offer, analysing the reasons for such variances. Also, by performing the wind tunnel experiment, it has been possible to verify the results obtained with the CFD, since similar tendencies and general functioning have been obtained. As a summary of these results it can be confirmed that:

- Aerofoils offer a greater maximum lift coefficient than finite wings.
- Aerofoils stall at lower angle of attack than finite wings.
- The slope of the lift curve for an aerofoil is greater than the one for a finite wing.
- The drag coefficient is greater in a finite wing due to the appearance of wing tip vortices.
- As a consequence of all these statements, the aerodynamic efficiency is greater for an aerofoil than for a finite wing.

Costs

This chapter analyses the costs associated to the development of the project. This approximation will provide an idea on the balance and order of magnitude at which aeronautical projects are being developed.

Thus, two main types of resources have been found along the process. The first one are the human resources, which includes:

- 1 Senior Lecturer.
- 1 Graduate Teaching Assistant.
- 1 Manufacturer Technician.
- 1 Wind Tunnel Assistant.
- 1 Aerospace Engineering Student.

The second one is related to the physical material that has been used. This group includes:

- Software Licence.
- Physical resources such as attachments and printing material.
- Computational Resources.

Tables 5 and 6 summarise the costs derived from the present project (Ferrero 2017).

Table 5. Cost derived from human resources.

	Number	**Hourly Rate (£)**	**Time (h)**	**Total (£)**
Senior Lecturer	1	30	15	450
Graduate Teaching Assistant	1	10	4	40
Manufacturer Technician	1	10	1	10
Wind Tunnel Assistant	1	6	2	12
Aerospace Engineering Student	1	26	210	5460
Total				£5972

Table 6. Cost derived from physical resources.

	Number	**Price (£)**	**Quantity**	**Total (£)**
StarCCM+ License	1	2.65	100 (h)	265
3D printing material	1	25	0.48 (g)	12
Laptop	1	700	4 (%)	25
Metal Bar and Attachments	1	0.5	3 (units)	1.5
Gorilla Glue	1	18.99	0.01 (l)	0.19
Fusion Autodesk	1	0.08	3 (h)	0.25
Microsoft Office Professional	1	465	25 (%)	116.25
Total				£420.19

All the values used to calculate salaries and unitary costs have been applied considering average market values and general licences.

Thus, the cost of the project is: £6392.19

 # SIX THOUSAND, THREE HUNDRED AND NINETY TWO POUNDS WITH NINETEEN PENCE #

Recommendations for further work

Regarding further investigations related to Lanchester's aerofoil, the following suggestions are made:

- Consideration of the application of the LAN1897 aerofoil to commercial aircrafts.
  It would imply the study of the aerofoil under compressible flow. Higher velocities would be used and atmospheric conditions would be changed according to the model chosen: International Standard Atmosphere (ISA), Miele's or Hale's, amongst others.

- Study of the aerofoil by means of different turbulent models.
  In this dissertation, only the Spalart Allmaras turbulent model has been used. Nevertheless, it would be interesting to test the different models that CFD tools provide (k-ε, k-ω) to observe the variations provoked by the turbulent model chosen.

- 3D study of the wing.
  Perform the CFD and wind tunnel analysis again, using a 3D model for the simulations. By doing so, it would be possible to understand the effects of the 3D span and compare the results in a quantitative manner. Application of the 3D corrections (Bak, Johansen and Andersen 2006).

- Improvement and comparison of the aerofoil.
  Deep comparison between the LAN1897 aerofoil and modern aerofoils such as supercritical aerofoils and NACA models. Improvement by applying features developed during the last years.

References and Bibliography

Aerofoil - Aviationknowledge (2019) available from <http://aviationknowledge.wikidot.com/aviation:aerofoil>

Allmaras, S. R., Johnson, F. T., and Spalart, P. R. (2012) ‘Modifications and Clarifications for the implementation of the Spalart-Allmaras Turbulence Model’. Seventh International Conference on Computational Fluid Dynamics.

Almohammadi, K., Ingham, D., Ma, L. and Pourkashan, M. (2013) ‘Computational Fluid Dynamics (CFD) Mesh Independency Techniques for a Straight Blade Vertical Axis Wind Turbine’. *Energy* 58, 483-493

Anderson, J. D. (2011), *Fundamentals of Aerodynamics*. 5th edn. McGraw-Hill.

Bak, C., Johansen, J., and Andersen, P. B. (2006) ‘Three-Dimensional Corrections of Airfoil Characteristics Based on Pressure Distributions’. European Wind Energy Conference & Exhibition.

Contel, A. (2016) Detached-Eddy Simulation of a Wall-Mounted Cylinder Flow. Unpublished BSc thesis. Germany: Technische Universität München.

Ferrero Micó, J. (2017) CFD study and manufacturing of a wing with winglets. Unpublished BSc thesis. Spain: Universitat Politècnica de València.

Frederick Lanchester Collection (2019) available from https://catalogue.lanchesterinteractive.org/records/LAN

Frederick William Lanchester | British Engineer (2019) available from <https://www.britannica.com/biography/Frederick-William-Lanchester>

Fouad Kandil, M. A. and Okasha Elnady, A. (2017) ‘Performance of GOE-387 Airfoil Using CFD’. International Journal of Aerospace Sciences 2017, 5(1): 1-7. DOI: 10.5923/j.aerospace.20170501.01

García-Cuevas González, L. M., and Quintero Igeño, P. M. (2018) ‘Aerodynamic II lecture notes’. Universitat Politècnica de València.

Govardhana, M., and Reddy, B. V. (2014) ‘Estimation of drag and lift on Ahmed Body Using CFD Analysis’. *International Journal of Advanced and Innovative Research* (2278-7844), 51 (3).

Guerrero, J. E., Maestro, D. and Bottaro, A. (2012) ‘Biomimetic Spiroid Winglets For Lift And Drag Control’. *Comptes Rendus Mécanique* 340 (1-2), 67-80.

Hortsmann, K. H., and Boermans, L. M. M. (2003) ‘Evolution of airfoils for sailplanes’ *Technical Soaring* [online] (27).

Inclination Effects On Drag (2019) available from <https://www.grc.nasa.gov/www/k-12/airplane/inclind.html>

Jarrett P. (2014) ‘F. W. Lanchester and the Great Divide’. *Journal of Aeronautical History.*

Jumper, E., Schreck, S. and Dimmick, R. (1987) ‘Lift-Curve Characteristics For An Airfoil Pitching At Constant Rate’. *Journal of Aircraft 24 (*10), 680-687

Lanchester, F. W. (1915) ‘The Flying Machine: The Aerofoil In The Light Of Theory and Experiment’. *Proceedings of the Institution of Automobile Engineers* 9 (2), 171-259.

Lanchester, G. H. (1955) ‘F. W. Lanchester, LL.D, F.R.S., His Life and Work’. *Transactions of the Newcomen Society*, 30 (1), 221-237. DOI: 10.1179/tns.1955.015

Marco Gimeno, J. (2017) Estudio computacional de un ala y sus partes móviles en condiciones realistas de vuelo [‘Computational study of a wing and its moving parts in realistic flight conditions’]. Unpublished BSc thesis. Spain: Universitat Politècnica de València.

Martínez Romá, M. (2018) Estudio paramétrico mediante CFD de la aerodinámica de un ala cerrada [Parametric study by CFD of the aerodynamics of a closed wing]. Unpublished BSc thesis. Spain: Universitat Politècnica de València.

Meshing -- CFD-Wiki, The Free CFD Reference (2019) available from <https://www.cfd-online.com/Wiki/Meshing>

Patel, K. S., Patel, S. B., Patel, U. B. and Ahuja, A. P. (2014) ‘CFD Analysis of an Aerofoil’. *International Journal of Engineering Research* [online] 3(3): 154-158. available from www.uvpce.ac.in

Puttkammer, P. P. (2013) Boundary Layer over a Flat Plate. Unpublished BSc thesis. The Netherlands: University of Twente.

Serdar Genç, M., Karasu Ilyas and Hakan Açikel, H. (2012) ‘An experimental study on aerodynamics of NACA2415 aerofoil at low Re numbers’. *Experimental Thermal and Fluid Science*: 252-264. available from www.elsevier.com/locate/etfs

Shaari, K. Z. K., and Awang, M. (2015) *Engineering Applications of Computational Fluid Dynamics*. Springer

Spalart, P. R., and Allmaras, S. R. (1992) ‘A One-Equation Turbulence Model for Aerodynamic Flows’. *Thirtieth Aerospace Sciences Meeting & Exhibit*.

Team, L. (2019) *Computational Fluid Dynamics (CFD) Blog - LEAP Australia & New Zealand | Tips & Tricks: Convergence And Mesh Independence Study* [online] available from <https://www.computationalfluiddynamics.com.au/convergence-and-mesh-independent-study/>

The Development of Aerofoils and Aerofoil Technology (2019) available from http://www.century-of-flight.net/Aviation%20history/evolution%20of%20technology/Airfoils.htm

The Enigma of the Aerofoil: Rival Theories In Aerodynamics, 1909-1930 - PDF Free Download (2019) available from <https://epdf.tips/the-enigma-of-the-aerofoil-rival-theories-in-aerodynamics-1909-1930.html>

The Science Behind Golf-Ball Dimples (2019) available from <https://medium.com/@jackeytrolololol/the-science-behind-golf-ball-dimples-fcdb9677929b>

Thévenin, D., and Janiga, G. (ed.) (2008), *Optimization and Computational Fluid Dynamics*. Springer.

Ugwueze, O. (2017) Flight Simulation Model of the Lanchester 1897 Manned Aerial Machine. Unpublished MSc thesis. United Kingdom: Coventry University

Valero Paredes, S. (2016) Aplicación de Tobera convergente en un perfil [Application of a convergent nozzle in an aerofoil]. Unpublished BSc thesis. Spain: Universitat Politècnica de València.

Wendt, J. F. (ed.) (2009), *Computational Fluid Dynamics*. Springer.

3 Criteria For Assessing CFD Convergence (2019) available from https://www.engineering.com/DesignSoftware/DesignSoftwareArticles/ArticleID/9296/3-Criteria-for-Assessing-CFD-Convergence.aspx

Appendices

A1. LAN1897 Aerofoil Data

Upper surface

X	Y
1.00000000	-0.01118816
0.97212612	-0.01015319
0.94425225	-0.00767290
0.91647722	-0.00579052
0.88880103	-0.00288139
0.86092715	0.00054112
0.83325096	0.00447521
0.80547593	0.00896444
0.77760206	0.01375295
0.75002471	0.01943930
0.72215084	0.02497601
0.69437580	0.03111128
0.66669962	0.03784512
0.63872690	0.04398040
0.61095186	0.04996603
0.58327568	0.05729843
0.55540180	0.06415797
0.52772561	0.07196324
0.49985174	0.07944528
0.47217555	0.08695146
0.44440051	0.09411008
0.41662548	0.09904823
0.38885045	0.10442648
0.36117426	0.10697919
0.33320154	0.10952309
0.30552535	0.11089077
0.27775032	0.11246101
0.24997529	0.11089077
0.22200257	0.10860529
0.19432638	0.10442648
0.16655135	0.09606886
0.13897400	0.08695146
0.11119897	0.07593461
0.08332510	0.06415797
0.05555006	0.04896230
0.02777503	0.03162691
0.00412300	0.01031000
0.00040000	0.00414600
0.00000000	0.00000000

Lower surface

X	Y
0.00000000	0.00000000
0.00500000	-0.00150000
0.01111000	-0.00142200
0.02777503	0.00054112
0.05555006	0.00549510
0.08332510	0.01034813
0.11119897	0.01452421
0.13897400	0.01747802
0.16655135	0.02094110
0.19432638	0.02297821
0.22200257	0.02497601
0.24997529	0.02572831
0.27775032	0.02572831
0.30552535	0.02572831
0.33320154	0.02572831
0.36117426	0.02497601
0.38885045	0.02497601
0.41662548	0.02297821
0.44440051	0.02094110
0.47217555	0.01849657
0.49985174	0.01595019
0.52772561	0.01309823
0.55540180	0.01034813
0.58327568	0.00719061
0.61095186	0.00342196
0.63872690	0.00054112
0.66669962	-0.00288139
0.69437580	-0.00579052
0.72215084	-0.00767290
0.75002471	-0.01015319
0.77760206	-0.01118816
0.80547593	-0.01384950
0.83325096	-0.01518017
0.86092715	-0.01621514
0.88880103	-0.01621514
0.91647722	-0.01621514
0.94425225	-0.01518017
0.97212612	-0.01384950
1.00000000	-0.01118816

A2. Mesh independence

Complete data obtained from the eight meshes studied to prove the independence of the mesh chosen is provided in this Appendix. Table 7 illustrates the values for the forces, force coefficients and moment in the different meshes.

Table 7. Parameters for mesh independence.

Mesh number	Cells	C_D (-)	C_L (-)	M (N·m)	D (N)	L (N)
1	2573	0.2606	1.3162	86.4670	52.1140	263.2319
2	6862	0.2379	1.2846	82.7997	47.5826	256.9194
3	10044	0.2368	1.2883	82.1676	47.3541	257.6526
4	16353	0.2016	1.3098	83.3761	40.3280	261.9672
5	17448	0.1998	1.3007	82.7004	39.9591	260.1412
6	20372	0.1989	1.3217	85.1686	39.7894	264.3347
7	27094	0.2078	1.3008	85.3580	41.5617	260.1537
8	28740	0.2015	1.2837	83.2517	40.3049	256.7464

Also, another important process to undertake is calculating the imbalance and variation of mass flow. According to the continuity equation, mass must be kept constant along the process, meaning that the mass flow at the inlet and the outlet must be the same. Table 8 shows such imbalances and variations of the mass flow.

As it can be seen, both the imbalance and the variation of the mass flow have an order of magnitude between 10^{-5} and 10^{-7}, so it could be concluded that mass was conserved.

Table 8. Mass Flow conservation.

Mesh	MassFlow - inlet	Mass Flow - outlet	Sum	Imbalance	Variation
1	447.2742	447.2973	894.5715	2.58224E-05	5.16462E-05
2	447.7059	447.7060	895.4119	1.11680E-07	2.23361E-07
3	447.7723	447.7943	895.5666	2.45655E-05	4.91321E-05
4	447.7838	447.7895	895.5733	6.36464E-06	1.27294E-05
5	447.7838	447.7895	895.5733	6.36464E-06	1.27294E-05
6	447.7801	447.7803	895.5604	2.23324E-07	4.46648E-07
7	447.7800	447.7809	895.5609	1.00496E-06	2.00992E-06
8	447.7843	447.7845	895.5688	2.23322E-07	4.46644E-07

A3. Convergence

Convergence is said to be achieved when the three criteria stated in Section 5.2.1 are accomplished. Thus, this appendix provides evidence of convergence for some of the simulations of the project:

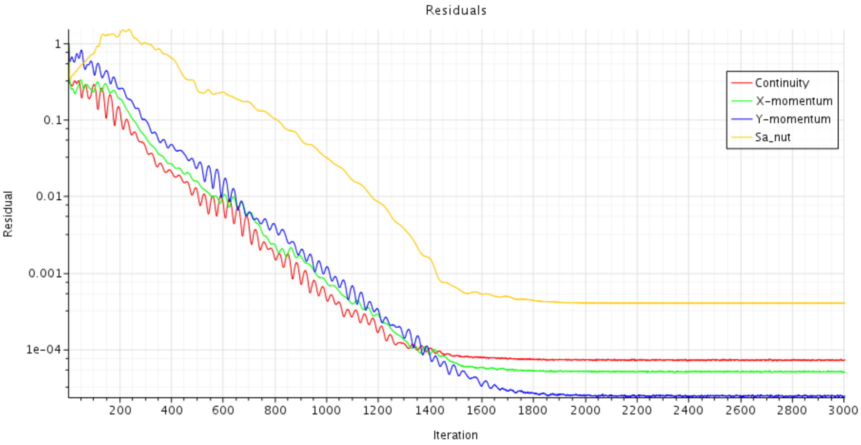

Figure 41. Residuals at constant velocity and at an angle of attack α = 0°.

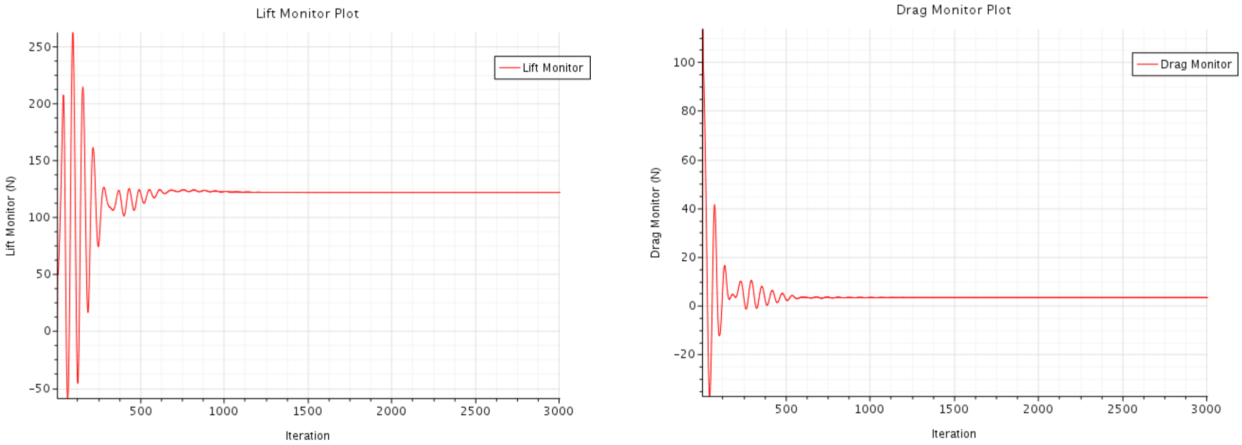

Figure 42. Lift and Drag monitor plots at constant velocity and at an angle of attack α = 0°.

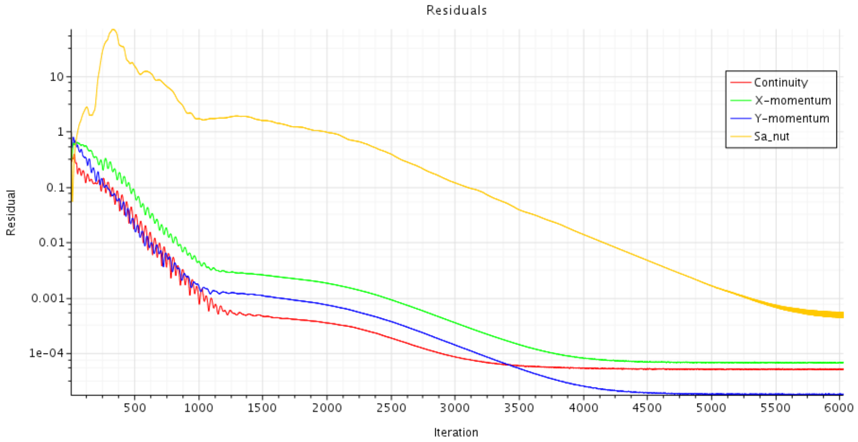

Figure 43. Residuals at constant velocity and at an angle of attack α = 10°.

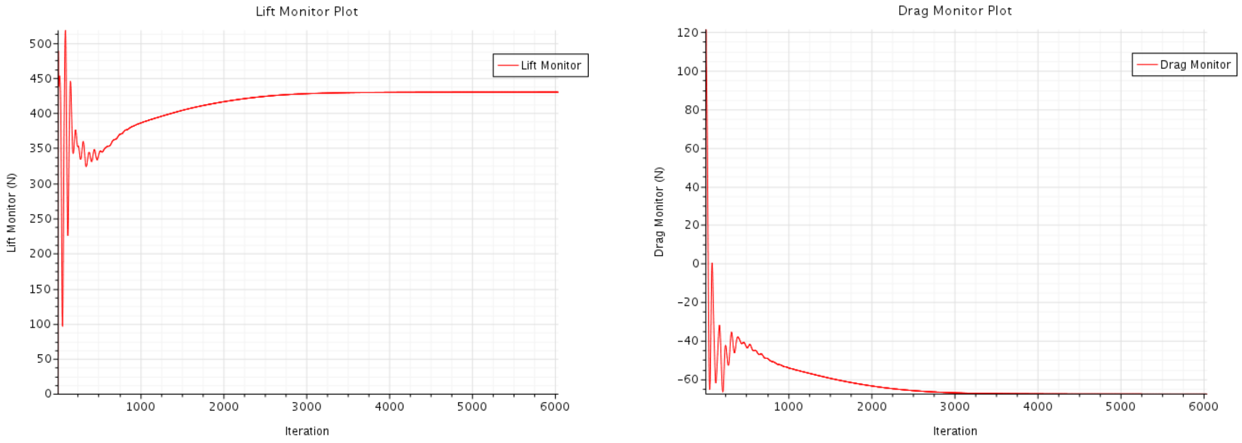

Figure 44. Lift and Drag monitor plots at constant velocity and at an angle of attack α = 10°.

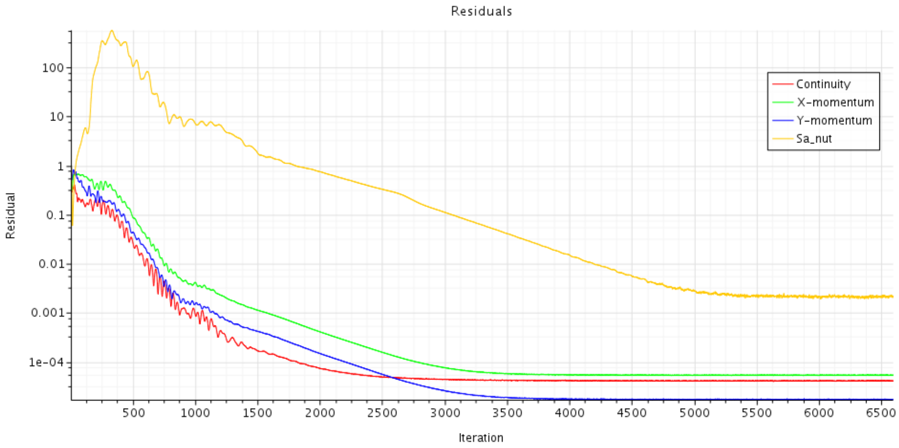

Figure 45. Residuals at constant velocity and at an angle of attack α = 15°.

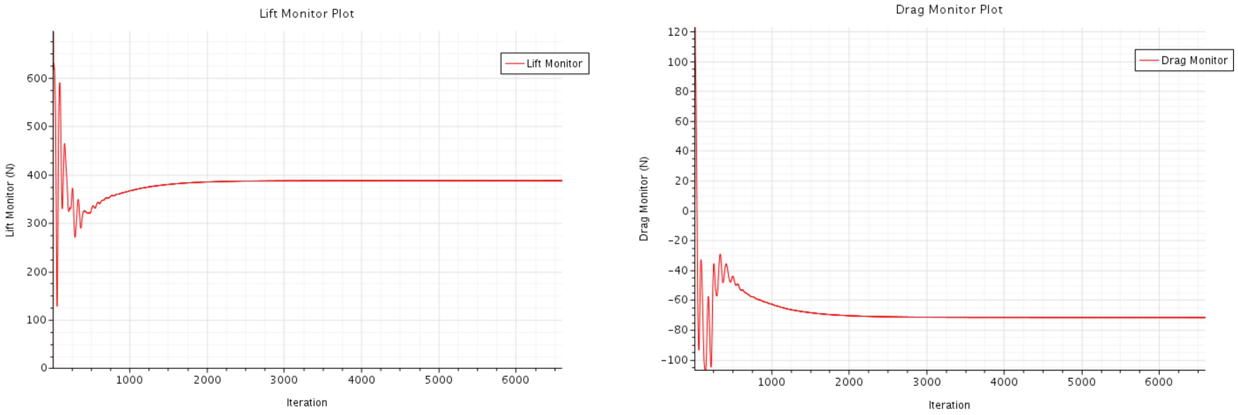

Figure 46. Lift and Drag monitor plots at constant velocity and at an angle of attack α = 15°.

A4. Velocity determination

To determine the velocity at which the experiments must be undertaken in order to obtain valid results, it is necessary to maintain the Reynolds number constant. To do so, the model scale is taken into account – 1:10 – and both the dynamic viscosity and the density are assumed to be exactly the same.

In this appendix, the calculations are shown:

$$\mathrm{Re_m} = \mathrm{Re_R} \rightarrow \frac{\rho_\mathrm{m}\,\mathrm{D_m}\,\mathrm{V_m}}{\mu_\mathrm{m}} = \frac{\rho_\mathrm{R}\,\mathrm{D_R}\,\mathrm{V_R}}{\mu_\mathrm{R}} \rightarrow \{\rho_\mathrm{m} = \rho_\mathrm{R};\, \mu_\mathrm{m} = \mu_\mathrm{R}\} \rightarrow \mathrm{D_m}\,\mathrm{V_m} = \mathrm{D_R}\,\mathrm{V_R}$$

$$\left\{\mathrm{D_m} = \frac{1}{10}\mathrm{D_R}\right\} \rightarrow \frac{1}{10}\mathrm{D_R}\,\mathrm{V_m} = \mathrm{D_R}\,\mathrm{V_R} \rightarrow \mathrm{V_m} = 10\mathrm{V_R}$$

Therefore, the velocity in the wind tunnel must be 10 times the velocity of the simulations.

A5. CFD numerical results

This appendix summarises the numerical values that were obtained from the simulations to elaborate Figures 15 and 16.

Table 9. CFD parameters at constant velocity.

AoA (°)	Normal (N)	Axial (N)	Lift (N)	Drag (N)	C_L (-)	C_D (-)
-10	-142.5948	13.8607	-138.0216	38.4115	-0.4589	0.1277
-5	-68.4577	11.6917	-67.1782	17.6137	-0.2233	0.0586
0	121.8067	3.3903	121.8067	3.3903	0.4050	0.0113
3	220.4349	-7.8491	220.5436	3.6983	0.7332	0.0123
5	285.2246	-20.5686	285.9319	4.3686	0.9506	0.0145
8.6	394.6124	-53.3060	398.1467	6.3019	1.3237	0.0210
10	429.8013	-67.6397	435.0171	8.0222	1.4463	0.0267
12	433.0530	-67.9943	437.7266	23.5283	1.4553	0.0782
15	387.3984	-71.6337	392.7383	31.0732	1.3057	0.1033
20	362.3440	-67.9965	363.7482	60.0332	1.2094	0.1996

Next, Table 10 summarises the parameters obtained at a constant angle of attack of 0°.

Table 10. CFD parameters at constant angle of attack.

Velocity (m/s)	Drag (N)	Lift (N)	C_D (-)	C_L (-)
5	0.2910	6.3357	0.0190	0.4138
10	0.8809	24.9987	0.0144	0.4081
15	1.7476	55.9210	0.0127	0.4058
20	2.8489	99.2936	0.0116	0.4053
22.16	3.3903	121.8067	0.0112	0.4049
25	4.1632	154.8379	0.0109	0.4045
30	5.6671	222.4922	0.0103	0.4036
35	7.3730	302.1976	0.0098	0,4028

A6. Wind Tunnel numerical results

This Appendix summarises the numerical values that were obtained from the wind tunnel, together with the calculations of the lift, drag and moment coefficients.

Constant Velocity

Table 11. Wind Tunnel parameters at constant velocity.

	Test 1	Test 2	Test 3	Test 4	Test 5	Test 6
Angle of Attack (°)	0	5	10	15	18	-5
Data Section Time (sec)	348.3000	348.3000	348.3000	348.3000	348.3000	348.3000
Begin Sample	48.0000	81.0000	103.0000	124.2000	146.2000	182.3000
Data Section	1.0000	1.0000	1.0000	1.0000	1.0000	1.0000
Data Section Time (sec)	348.3000	348.3000	348.3000	348.3000	348.3000	348.3000
End Sample	58.1000	91.2000	112.9000	134.3000	156.2000	192.0000
Sample Number (user defined)	0.9944	1.9945	2.9943	3.9944	4.9944	5.9942
Temperature Ambient Tunnel Hall (°C)	21.1577	21.1236	21.1252	21.1265	21.0969	21.0860
Temperature Tunnel Air Temp (°C)	20.7935	20.8926	20.9544	20.9753	20.9872	21.0355
Pressure Ambient Tunnel Hall (mbar)	980.8011	980.7987	980.7973	980.8131	980.7982	980.7923
Air Density (kg/m3)	1.1624	1.1620	1.1618	1.1617	1.1616	1.1614
Pressure Dynamic Pitot Static (Pa)	0.2947	0.1372	0.3756	0.2533	0.5240	0.3630
Pressure Dynamic Contraction (Pa)	257.9036	257.3968	257.0018	256.4769	256.3953	256.4278
Fan Speed (rpm)	504.2424	504.2424	504.2473	504.2424	504.2473	504.2424
Wind Speed Syn (m/s)	21.6776	21.6599	21.6456	21.6241	21.6212	21.6244
Wind Speed Pitot (m/s)	0.6312	0.4498	0.7558	0.6154	0.8713	0.7308
Pitch Angle Actual (°)	0.0000	0.0000	0.0000	0.0000	0.0000	0.0000
Yaw Angle Actual (°)	0.0000	0.0000	0.0000	0.0000	0.0000	0.0000
Drag Force (N)	1.7469	1.8912	2.8537	3.6446	4.1088	2.1867
Side Force (N)	5.1793	4.7762	4.7908	4.1556	4.1768	5.0370
Lift Force (N)	-4.8473	-11.3667	-15.0308	-17.8084	-17.2667	1.0118
Pitch Moment (Nm)	-1.3152	-1.7959	-2.6930	-3.6282	-4.0085	-1.4745
Roll Moment (Nm)	3.2764	2.9932	2,.7729	2.5663	2.5651	3.1932
Yaw Moment (Nm)	-0.1207	-0.1034	-0.0701	-0.0870	-0.0774	-0.1181
Resolved Force X (N)	1.7469	1.8912	2.8537	3.6446	4.1088	2.1867
Resolved Force Y (N)	5.1793	4.7762	4.7908	4.1556	4.1768	5.0370
Resolved Force Z (N)	-4.8473	-11.3667	-13.0308	-17.8084	-17.2667	1.0118
Resolved Moment Pitch (Nm)	0.2134	-0.1411	-0.1960	-0.4391	-0.4133	0.4388
Resolved Moment Roll (Nm)	-1.2555	-1.1859	-1.4191	-1.0698	-1.0896	-1.2142
Resolved Moment Yaw (Nm)	-0.1207	-0.1034	-0.0701	-0.0870	-0.0774	-0.1181

Constant Angle of Attack

Table 12.Wind Tunnel parameters at constant angle of attack.

	Test 1	Test 2	Test 3	Test 4	Test 5	Test 6
Wind Speed Syn (m/s)	10.0070	15.0509	19.6919	24.6021	29.7085	34.6571
Data Section Time (sec)	290.0500	290.0500	290.0500	290.0500	290.0500	290.0500
Begin Sample	53.5000	89.1000	122.3000	185.1000	229.7000	274.2000
Data Section	1.0000	1.0000	1.0000	1.0000	1.0000	1.0000
Data Section Time (sec)	290.0500	290.0500	290.0500	290.0500	290.0500	290.0500
End Sample	63.5000	99.5000	132.5000	195.2000	239.4000	284.4000
Sample Number (user defined)	0.9944	1.9946	2.9945	3.9944	4.9942	5.9945
Temperature Ambient Tunnel Hall (°C)	21.0966	21.0959	21.0961	21.0539	21.0519	21.0055
Temperature Tunnel Air Temp (°C)	20.8757	20.8063	20.8722	21.1931	21.5028	22.0618
Pressure Ambient Tunnel Hall (mbar)	980.7256	980.7428	980.7272	980.6881	980.7317	980.7133
Air Density (kg/m3)	1.1620	1.1623	1.1620	1.1607	1.1595	1.1573
Pressure Dynamic Pitot Static (Pa)	0.3187	0.2927	0.4176	0.2975	0.4245	0.1551
Pressure Dynamic Contraction (Pa)	54.9420	124.3151	212.7459	331.7052	483.1920	656.3124
Fan Speed (rpm)	257.9394	359.7063	461.5306	571.3387	679.7526	786.6976
Wind Speed Pitot (m/s)	0.7060	0.6747	0.7576	0.6271	0.8045	0.5632
Pitch Angle Actual (°)	0.0000	0.0000	0.0000	0.0000	0.0000	0.0000
Yaw Angle Actual (°)	0.0000	0.0000	0.0000	0.0000	0.0000	0.0000
Drag Force (N)	0.5583	1.0402	1.4897	2.1096	2.8879	4.0536
Side Force (N)	0.4496	3.2539	4.5569	5.8568	7.1786	8.5190
Lift Force (N)	-0.7921	-2.4561	-4.4272	-7.4425	-15.3127	-27.9296
Pitch Moment (Nm)	-0.4034	-0.7768	-1.1440	-1.6728	-2.5493	-3.9970
Roll Moment (Nm)	0.2448	2.0477	2.9067	3.7226	4.6073	5.3928
Yaw Moment (Nm)	-0.0046	-0.0646	-0.0946	-0.1368	-0.1823	-0.2278
Resolved Force X (N)	0.5583	1.0402	1.4897	2.1096	2.8879	4.0536
Resolved Force Y (N)	0.4496	3.2539	4.5569	5.8568	7.1786	8.5190
Resolved Force Z (N)	-0.7921	-2.4561	-4.4272	-7.4425	-15.3127	-27.9296
Resolved Moment Pitch (Nm)	0.0852	0.1334	0.1595	0.1731	-0.0224	-0.4501
Resolved Moment Roll (Nm)	-0.1486	-0.7994	-1.0806	-1.4020	-1.6740	-2.0614
Resolved Moment Yaw (Nm)	-0.0046	-0.0646	-0.0946	-0.1368	-0.1823	-0.2278